Master thesis

Optical characterisation of femtosecond Laser-induced periodic surface structures fabricated on stainless steel substrate material utilising static linearly polarised laser pulses

seit 1558

In order to obtain the academic degree "Master of Science" (M. Sc.) in the course of the study of Photonics at the Friedrich Schiller University Jena

Theophilus Kobina Sarpey (B. Sc.)

Born in Axim

Jena, 15th March, 2016

The following work was made from October 2015 to March 2016 in the Otto Schott Institute for Materials Research in the working group Surface and Interface Technology, “Oberflächen- und Grenzflächentechnologie” at the Friedrich Schiller University of Jena.

Primary supervisor	Prof. Dr.-Ing. habil. Frank A. Müller
Second supervisor	Dr. rer. nat. Stephan Gräf

Table of Contents

1 INTRODUCTION

Prior to the first use of ultrafast laser pulses (particularly, femtosecond laser pulses in this case) in the processing of materials, several approaches were then employed. The advent of femtosecond laser has opened a new era for micro- and nano-machining of various materials [1]. Laser-induced periodic surface structures (LIPSS) also known as ripples, are the periodic features that emerge on the surface of materials after irradiation with one or a multiple of laser pulses and some pulse duration with fluences near the material ablation threshold [2].

Laser-induced periodic surface structures (LIPSS) has been a research hotspot following their discovery some five decades ago by Birnbaum [3] when he utilised pulsed ruby laser to irradiate semiconductors. After this discovery, quite a number of research works have been performed and have thus confirmed the versatility associated with the generation of LIPSS using ultrafast laser pulses especially femtosecond (fs) pulses. This makes LIPSS feasible to be fabricated on all classes of materials (metals [4], semiconductors [5, 6], dielectrics [7], ceramics [8], polymers [9, 10]) when irradiated near their ablation threshold. Laser-induced periodic surface nanostructures provide a new method for changing the metallic optical properties for various purposes, and have great potential applications in plasmonic enhanced optoelectronics devices for improved solar energy (photovoltaic cells) and optical sensitive elements [11]. This is normally brought into perspective when the optical path length of the incident light is greatly enhanced and hence reduces surface reflection following the surface texturing and thus it has become indispensable for solar cells [12].

Ripple formation may be applied in the fabrication of gratings, shallow junctions of metal-oxide-silicon transistors and liquid-crystal displays and to texture magnetic recording media (optical memories) [13]. LIPSS also has wide range of applications in surface topographies for biomedical applications [14], tribology [15], surface incandescent light sources [16], photoelectron emission [17], tailoring of surface wettability properties [18], blackening of metals and silicon [19, 20] and nanostructure formation for surface colourising [21]. A ripple structure could also be used to roughen the surface of micro-electro-mechanical systems (MEMS) components so as to enhance its surface adhesion and improve the performance of lift time of micro-devices [22].

Based on the numerous applications and high interest of LIPSS, it has become quite necessary to know and confirm the origin of these micro/nano-structures and as such many research works have accepted that there exists low spatial frequency LIPSS (LSFL) as well as high

spatial frequency LIPSS (HSFL) structures. LSFL structures have period Λ close to the initial laser wavelength λ with grating vector perpendicular to the polarisation of the laser field in most cases especially for high absorbing materials. In contrast, HSFL have period Λ in the range of $\lambda/2$ to $\lambda/20$ of the initial laser wavelength λ. The grating vector for these structures is either parallel or perpendicular to the polarisation of the laser field [22].

With most of the work in the generation and characterisation of all types of LIPSS at appropriate conditions performed utilising polished stainless steel samples [23, 24] coupled with its numerous industrial applications such as in chemical, processing, oil and gas, power generation, architecture, building and construction, medical and automobile [25], as well as its low cost among others, it was thus imperative and expedient to have settled on stainless steel as our sample so as to confirm (agree or disagree with) other investigations.

A detailed investigation of the optical behaviour of LSFL samples in relation to their fabricating polarisation states is of crucial significance. This would enable us to comprehend the light trapping efficiency of solar cells and also the absorption enhancement of LSFLs generated on metallic substrates because of the intrinsic high reflectance of metals. Several laser polarisation states (static – linearly, elliptically and circularly polarised as well as dynamic) have been extensively employed by numerous authors [26, 27] in the fabrication of LIPSS. However, just a few of them have performed an in-depth optical investigation. Li et al [12] investigated the colour effect of fs LIPSS generated on stainless steel substrate material by utilising them as gratings. Vorobyev et al [28] reported the spectral reflectance of LIPSS on silver Ag using the integrating sphere with both polarised and unpolarised light source. In another paper [29], they studied the low reflectance enhancement on multifunctional LIPSS fabricated on brass, platinum Pt and titanium Ti. However, all these studies were performed using only total reflectance spectra. Lee et al [30] performed both total and diffuse reflectance investigation on uncoated stainless steel as well as stainless steel coated with silver Ag film. Their work was more focused on illustrating the relation between the wavelength dependent reflectance by using different samples with varying gaps and diameters. Their structures were also fabricated using photolithography and wet-chemical etching hence the fluence dependence as well as other laser fabricating parameters considered in LIPSS fabrication were not dealt with. In spite of all these numerous advancements in optical property investigations of LIPSS, a study on (diffuse, total and specular reflectance) utilising both static and dynamic polarisation states have not yet been performed to the best of our knowledge.

On the basis of the earlier outlined studies, the aim of this work therefore encompasses the generation of LIPSS (LSFL) on polished stainless steel substrate materials. This would be done by employing static linearly polarised fs laser pulses at a fundamental wavelength λ of 1025 nm, pulse duration τ of 300 fs and a repetition rate f_{rep} of up to 100 kHz maximum, in ambient air environment. Thereafter, a study of the optical properties of the laser irradiated samples (LIPSS) in relation to their surface morphology would be performed. The optical parameters such as the wavelength of the laser beam (fundamental) as well as the wavelength of the incident unpolarised white light source would be investigated. The incident angles 0° and 8° corresponding to diffuse and total reflectance respectively of the unpolarised white light source with respect to the LIPSS and the detector would also be varied and investigated thoroughly. The reflectance measurements would be done with and without the use of an integrating sphere with a spectrophotometer. The morphology of the LIPSS samples would be characterised using scanning electron microscopy (SEM).

2 FUNDAMENTALS

In this section, particular emphasis is placed on the description of the basic concept behind the fabrication of LIPSS. The theory of the diverse polarisation states employed for the fabrication of LIPSS is elucidated further here. The basic phenomenon employed in characterising substrate materials (total reflectance measurements especially as well as diffuse and specular) utilising an integrating sphere is also described in some details.

2.1 BASIC CONCEPTS IN LIPSS FABRICATION

The laser-material interaction leading to the formation of LIPSS depends on laser irradiation conditions such as laser wavelength, laser pulse duration, laser energy (fluence), number of laser pulses applied (scanning velocity), polarisation direction of the laser field among others [31]. The laser-material interaction also depends on material properties like electron-phonon relaxation strength, electronic diffusion, energy band characteristics of the electronic laser excitation [31].

LSFL structures are mainly believed to form as a result of interference effects arising from the incident laser radiation and the surface-induced electromagnetic waves (surface plasmon polaritons SPPs especially for the case of metals and even for higher intensities, semiconductors and dielectrics). Other factors which also contribute to this observed interference effects are the surface roughness and isolated defects [32, 33]. The period Λ for LSFLs is given by the formula:

$$\Lambda = \frac{\lambda}{(1 \pm \sin\theta)} \tag{1}$$

Where λ is the initial laser wavelength and θ is the incident angle.

Using the arguably most accepted Sipe theory together with the Drude model and the surface plasmon polariton (SPP) excitation theory, the optical origin for the formation of LIPSS (LSFL to be precise) could be explained [32]. Other mechanisms for the formation of these micro/nano-ripples especially for HSFLs are based on several theories such as these: surface instabilities or self-organisation [33], ultrafast non-thermal ablation mechanism or Coulomb explosion [34], change in refractive index, second harmonic generation (using in-situ method) [35, 36, 37], enhancement of localised electric field, melting, evaporation and resolidification governed by highly non-linear processes driven by surface capillary waves, surface tension and surface energy [38].

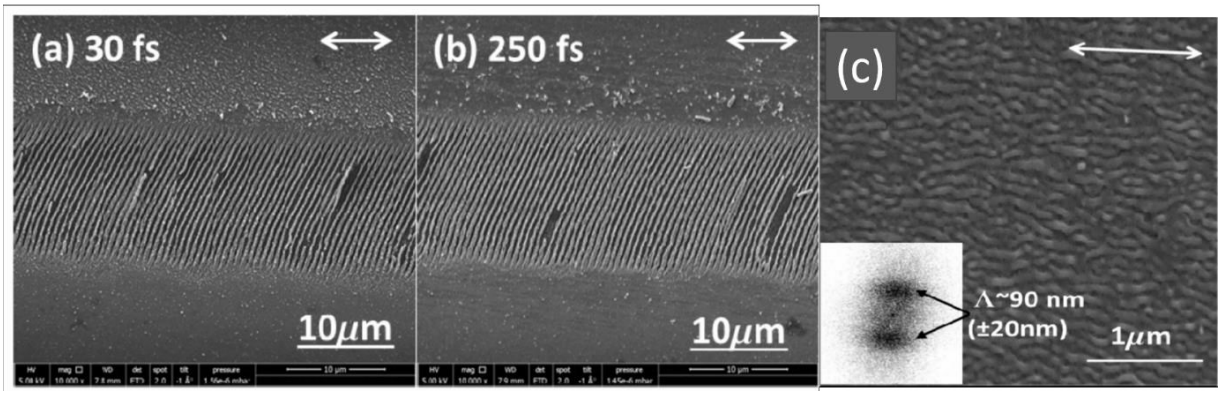

Figure 1: SEM micrographs of LIPSS fabricated on titanium film substrate. The double-headed arrow indicates the direction of the laser beam polarisation. (a) and (b) display LSFLs with different laser pulse durations while (c) represents HSFL with the same polarisation as the LSFLs [22].

The appearance and dependency of the periodicity of LSFLs are dependent on laser wavelength, laser fluence, number of laser pulses but independent of laser pulse duration. Figure 1 confirms that LSFLs can be generated utilising different laser pulse durations and yet exhibit almost similar morphological features. However, the appearance and dependency of the periodicity of HSFLs relies on laser fluence, pulse duration and slightly on the number of laser pulses but independent of laser wavelength [22]. This remark on the independence of the laser wavelength comes as a result of the HSFLs yielding the same range of periodicity after irradiating the titanium substrate with both the fundamental and second harmonic laser pulses [22]. The period Λ for the HSFLs depends on the nature of the material properties as well as the laser parameters utilised in the fabrication process.

Based on these differences and many more, it has been established that different phenomena must be responsible for generating HSFL structures. The actual origin of the physical mechanism responsible for the generation of HSFL, however, has not been very well explained and hence many investigations are ongoing to uncover it.

It is worth noting that LSFLs can be fabricated on the surfaces of materials with nanosecond [39, 40], picosecond [41, 42], femtosecond lasers (pulsed lasers) [43] or even with continuous wave lasers [44]. However, with femtosecond lasers the precision is impeccable. Also with high repetition rate and pulse duration, the LSFLs produced are of enormous quality: LIPSS produced by long-pulsed lasers have smooth features, whereas LIPSS densely covered with nanostructures are reported for fs-lasers [45] and all these are evident in figure 1.

2.2 STATIC POLARISED LASER PULSES FOR LIPSS FABRICATION

Static polarised irradiation is initiated whenever a particular chosen laser polarisation is maintained throughout the LIPSS fabrication process. Static laser polarisation can be in the form of linear, elliptical or circular polarised irradiation. For static linear polarisation, the direction of the *E*-field vector relative to the scanning velocity *v* can be adjusted parallel (α = 0°), perpendicular (α = 90°), and under many varying angles of α = 30°, -45°, 45° [27] by a manual rotation of the polariser. With this, the phase shift is normally zero. For circular polarisation, the direction of the *E*-field relative to the scanning velocity *v* is normally performed by employing a quarter waveplate. This retards the horizontal component of the polarisation vector by some phase shift of $\lambda/4$ (90°) relative to the vertical component. In the case of elliptical polarisation, the phase shift can assume any other value other than that for the linear and circular polarisation states.

It has been established from a study carried out to investigate the effect of polarisation on LIPSS formation at fluence of 1 J/cm^2 using silicon Si as the substrate material that the number of laser pulses *N* required to form LIPSS with circular and elliptical polarisation is higher than that required for linearly polarised laser irradiation [46]. In another study on the effect of polarisation, static linearly polarised light and elliptically polarised light as well as left and right circularly polarised light were used to irradiate a tungsten W substrate material [47]. In that study, the linearly polarised light formed LIPSS oriented perpendicular to the polarisation of the laser beam as is expected [27, 28]. The alignment of LIPSS were however, angled at +45° and -45° for left and right rotated circularly polarised laser beams. On the contrary, for the elliptically polarised laser beam the LIPSS were aligned perpendicular to its elongated axis as is also reported by [48]. Keilmann et al [48] further observed that the amplitude of the ripples decreased with ellipticity and in their case however, they observed no hint of a periodic structure when a circularly polarised laser beam (α = 90°) was utilised. This non periodic structure persisted even for a doubled number of laser pulses.

2.3 DYNAMIC POLARISED LASER PULSES FOR LIPSS FABRICATION

The ability to control and manipulate the state of polarisation of the incident beam is desirable as it allows better control of laser-material interactions. Dynamic polarised laser irradiation involves modifying the direction of a linear polarisation with time. This implies for instance greatly improving the quality of the fabricated structures by utilising a continuously rotating waveplate during laser micro or nanoprocessing [49].

First, as an intermediary step between static and dynamic polarised laser pulses for LIPSS fabrication, Jin et al [26] established in their studies that a highly controlled real-time nanostructuring of polished stainless steel samples was possible. They established this by employing a dynamical switching (with the help of spatial light modulators SLMs) between four specific polarisation states (linear horizontal and vertical, radial and azimuthal). This switching between the four polarisation states was however, discrete and not continuous. In the case of radial polarisation, the LIPSS generally points away from the centre of the laser spot. On the contrary, for azimuthal polarisation the LIPSS forms an almost circular pattern around the centre. Radial and azimuthal polarisations produce patterns that are orthogonal to each other as is the case for the horizontal and vertical linearly polarised generated LIPSS patterns. Figure 2 shows the SEM images for the four specific polarisation states they investigated.

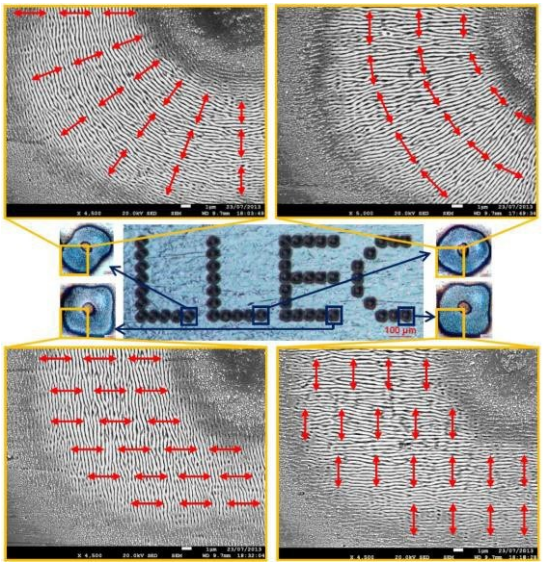

Figure 2: (Centre) Optical micrographs showing the processed geometry, which is produced by marking four distinct sets of laser spots, each set using a different state of polarization. (Top and bottom) magnified regions of laser spots, imaged with an SEM. The ablation spots had been produced either with a radially (top-left inlay), azimuthally (top-right inlay), horizontally (bottom-left) and vertically (bottom-right) polarized beam. The red arrows represent the direction of local electric field vectors [26].

Furthermore, Nayak and Gukpta [46] also employed radial polarisation in a polarisation state investigation on silicon. They noticed that with radial polarisation ripples are obtained much faster than with the other static polarisation states. They attributed this to the high number density of the ablated particle for radial polarisation at a given fluence compared to the other polarisation states.

Gräf and Müller [27] investigated the effect of the polarisation state during the formation of LIPSS mainly for LSFL. They established that tailored disordered surface morphologies could be obtained from static linear polarisation which initially had well-ordered periodic ripples. This was achieved by utilising a motor-driven rotation device to continuously rotate the electric field vector while the scanning velocity of the laser pulse is kept constant. The rotation of the polariser by means of the motor-driven rotation device in their setup gave a well-defined angle $\Delta\alpha$ (rotation angle between two successive pulses) each time as and when it was varied. They varied $\Delta\alpha$ between 2.9° and 28.8° but kept all other fabricating parameters especially the scanning velocity v fixed.

The SEM micrograph displayed in figure 3 further elucidates the increase in the order of randomness as $\Delta\alpha$ was increased. It was established that the dynamic polarised LIPSS at an angle of 28.8° is almost comparable to the LIPSS generated using a circular polarised laser source in terms of their morphological disorder. This further stresses the fact that the rotation period of the dynamic polarised LIPSS decreases with increasing $\Delta\alpha$. This decrease in the rotation period leads to a disordered pattern of the highest degree as $\Delta\alpha$ is increased. Normally, dynamic polarised LIPSS show the highest degree of disorder in comparison with static polarised LIPSS. However, the LIPSS fabricated utilising circularly polarised pulses illustrated in figure 3 showed the highest degree of disorder due to a slight deviation from the ideal LIPSS pattern normally observed when a circularly polarised laser pulse is used. The dynamic polarised LIPSS with the highest defined angle of $\Delta\alpha$ = 28.8° followed closely the circular polarised LIPSS and this was subsequently followed by $\Delta\alpha$ = 14.4°.

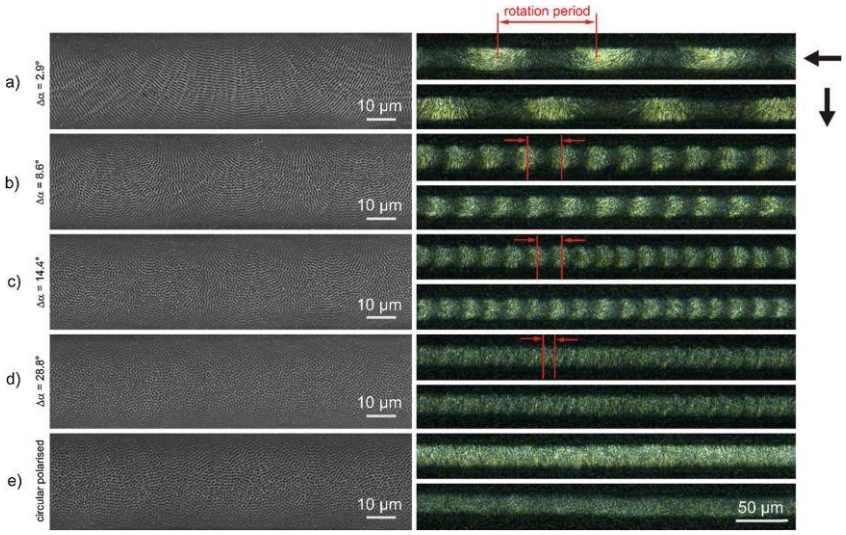

Figure 3: LIPSS generated at the surface of polished stainless steel samples with v = 0.5 mm/s, f_{rep} = 250 Hz and F = 1 J/cm² utilising an E-field vector rotating by an angle $\Delta\alpha$ of (a) 2.9°, (b) 8.6°, (c) 14.4° and (d) 28.8° in comparison to the utilisation of (e) circular polarisation; left: SEM micrographs and right: optical micrographs imaged with side-illumination at grazing incidence (arrows indicate the direction of illumination) [27].

Figure 4 reveals the general mechanism used in the generation of LIPSS utilising dynamic polarised pulses. In the generation of the initial LIPSS as a consequence of the interference of excited surface plasmons with the laser irradiation, the first of the required pulses always hit the unexposed region. The alignment of the pattern is actually related to the corresponding direction of the *E*-field vector. The energy of the subsequent laser pulses is then transferred to the metal surface by a grating-assisted coupling [50 - 54] and this leads to the generation of the final ripple pattern.

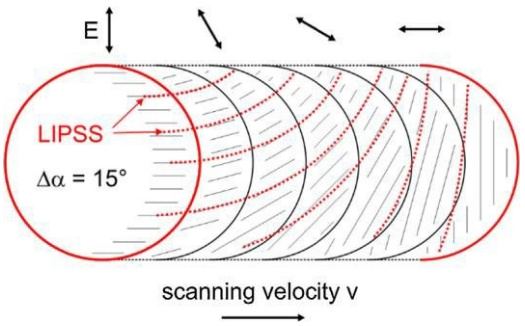

Figure 4: Formation mechanism of laser induced structures utilising an *E*-field vector continuously rotating with $\Delta\alpha$ = 15° between two successive laser pulses [27].

2.4 THEORY OF THE INTEGRATING SPHERE

Integrating spheres are highly reflective hollow enclosures that are placed in close proximity to the sample, such that the reflected light enters the sphere, bounces around the highly reflective diffuse surface of the sphere wall (inner diameter) and finally impinges upon the detector – usually part of the integrating sphere assembly. The name, integrating sphere, refers to one of the main functions of the device, namely that it spatially integrates the light flux [55]. In our application of the integrating sphere, the light would reflect from a stainless steel sample.

The integrating sphere acts like a Lambertian source (light falling on the surface is evenly scattered in all directions and the scattered light intensity is proportional to the cosine of the angle of observation) of diffuse light and at the same time, collects diffuse light reflected by the sample [56]. The reflectance measurements are based on the fact that the illumination intensity of the integrating sphere depend, besides on the input light output, also on the average reflectivity of its internal surface and then on the reflectance property of any sample held against one of its apertures [57]. A Teflon based polymer, Magnesium oxide MgO, Potassium bromide KBr, spectralon or Barium sulphate $BaSO_4$ could be used as the coating material in the integrating sphere. These materials operate normally at > 99% reflectance, 8° (standard angle of incidence used in commercial spectrophotometers for total reflectance measurements; at this angle, specular components of the sample reflection are removed by opening a special window).

Specular reflection takes place on a smooth surface, and the angle of incidence is the same as the angle of reflection. Diffuse reflection is a phenomenon where an incident beam of light strikes an uneven or granular surface and then scatters in all directions rather than in only one direction as in the case of specular reflection. It is also worth noting that an illuminated ideal-diffuse reflecting surface will have equal luminance from all directions which lie in the half-space adjacent to the surface (Lambertian reflectance). The diffuse reflectance spectrum is the compliment of the specular reflectance spectrum. The total reflectance spectrum is the sum of the specular and diffuse reflectance spectra [30]. Hence the specular reflectance can be evaluated from the total and diffuse reflectance measurements by a mere subtraction. A figure illustrating how to measure total and diffuse reflectance using an integrating sphere is given in figure 5.

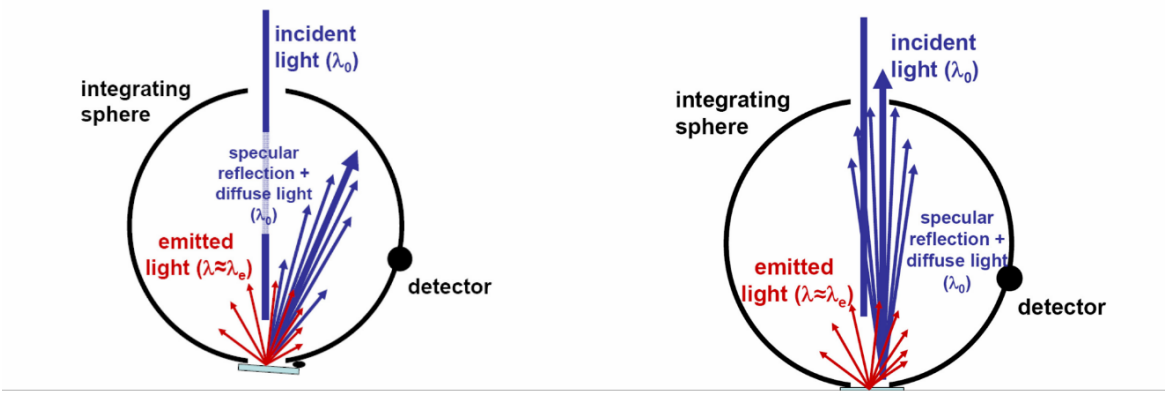

Sample tilted by about 8°

Sample not tilted

(a) Total reflectance

(b) Diffuse reflectance

Figure 5: Schematic diagram of the measurement procedure for total and diffuse reflectance using the integrating sphere [58].

Reflectance knowledge of the LIPSS samples enables us to obtain its internal spectral response, its absolute optical loss as well as to help in measuring the reflectance at different incidence angles and wavelengths. This allows knowing and then improving the light collection capabilities of the LIPSS sample with respect to the white light source. The integrating sphere collects all the light reflected by the sample and measures the respective total reflectance. The sphere also measures the diffuse reflectance when the specular reflected beam is selectively absorbed by a light trap [57]. In the measurement of total reflection, the normal of the sample is tilted by an angle of about 8° away from the direction of the incident light beam. This ensures that the direct reflected light is not reflected back to its source. It rather hits the wall of the integrating sphere and is scattered and eventually measured by the detector. In this process, specular as well as diffuse reflected light is detected [58]. Diffuse reflection in the integrating sphere occurs via a phenomenon described briefly here: Diffuse reflectance relies upon the focused projection of the spectrophotometer beam into the substrate material where it is reflected, scattered and transmitted through the substrate material. The back reflected light, diffusely scattered light (some of which is absorbed by the substrate material thereby making the light beam weaker) is then collected by the accessory and directed to the detector optics. The back reflected light is relevant and occurs in this case because the sample is not tilted. This also enables specular reflected light to escape undetected from the integrating sphere through the entrance opening and hence only diffuse reflected is captured by the detector [58]. Only the part of the beam that is scattered within the substrate material and returned to the surface is therefore considered to be diffusely reflected [59].

2.5 REFLECTANCE MEASUREMENT USING THE INTEGRATING SPHERE

Hou et al [60] used a pump-probe experiment and other methods to study the effect of pulse number on reflectance at two different laser fluences and for three substrate materials. Their work showed that reflectance increased with the formation of HSFL ripples. Ou et al [40] investigated the reflectance spectra dependency on the laser pulse fluence on stainless steel, brass and aluminium. They remarked that there exist different fluence dependencies in terms of femtosecond laser blackening of metals. They noted that the origin of the specific blackening fluence threshold for certain metals in the visible spectral range originates from the definite fluence threshold of femtosecond laser-induced ripples. Figure 6 further clarifies the laser fluence – reflectance dependence for the metal samples studied.

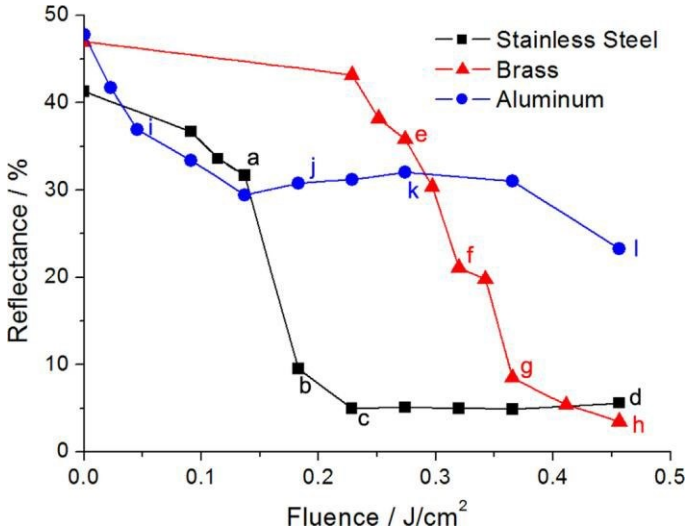

Figure 6: The arithmetic mean of the reflectance in the visible spectral range (400 – 750 nm) is plotted as a function of peak laser fluence for the irradiated surfaces of stainless steel, brass and aluminium [40].

Vorobyev and Guo [28] studied the spectral and polarisation responses of femtosecond laser-induced periodic surface structures on metals. Utilising polished silver substrate material before and after laser treatment, they observed about 85 – 95% surface absorption for the laser treated samples with the untreated samples showing higher reflectance for the wavelength range considered. The reflectance measurement was done at a fixed angle of incidence of 8°. They remarked that surface structuring with femtosecond LIPSS was a versatile technique for modifying optical properties in mainly the Ultraviolet (UV), Visible (Vis) and Near Infra-red (NIR) wavelength range by controlling the period of the femtosecond LIPSS. In subsequent papers, they used platinum and stainless steel metals and made similar inferences regarding the extent of the measured reflectance which was again in the range of 85 – 95% [1]. Yang et al [41] demonstrated that an ultra-broadband absorption of about 90% from ultraviolet to mid infra-red region had been achieved on TiNi surfaces through the production of coral-like

microstructures from femtosecond laser pulses. In another paper, Vorobyev and Guo [29] produced multifunctional surfaces using femtosecond pulses. Their work gives a more detailed understanding of how black metals could be used such that the efficiency of solar energy conversion into electricity and heat would receive a massive boost. Figures 7 (a) and (b) provide further information regarding the results obtained from the various reflectance measurements. Two polarised reflectance with the incident light polarisation E either parallel or perpendicular to the grating vector g of the LIPSS are displayed in Figure 7 (a). Comparing the untreated reflectance spectra with the reflectance spectra for the unpolarised light source, a clear reduction in reflectance was evident. This buttresses the fact that the laser irradiated polished samples always exhibit a reduction in their reflectance spectra in comparison to the untreated samples. Furthermore, it can be observed that the reflectance spectra of the LIPSS depend strongly on the polarisation state of the illuminating light source (unpolarised and polarised). There was a clear variation in the reflectance spectra amongst each of the investigated samples. From a comparison conducted between LIPSS investigated utilising polarised-light source with $g \parallel E$ and $g \perp E$, it was observed that the lowest reflectance spectra occurred when the LIPSS was illuminated with polarised light parallel to its electric field vector $g \parallel E$.

Figure 7 (b) further provides a remarkably clear difference in the reflectance spectra when polished unirradiated metallic samples are compared with the laser irradiated samples. These very low reflectance values of about 1.3% to 4.5% in the visible spectra range for the various metals were as a result of the pitch black appearance of the irradiated samples.

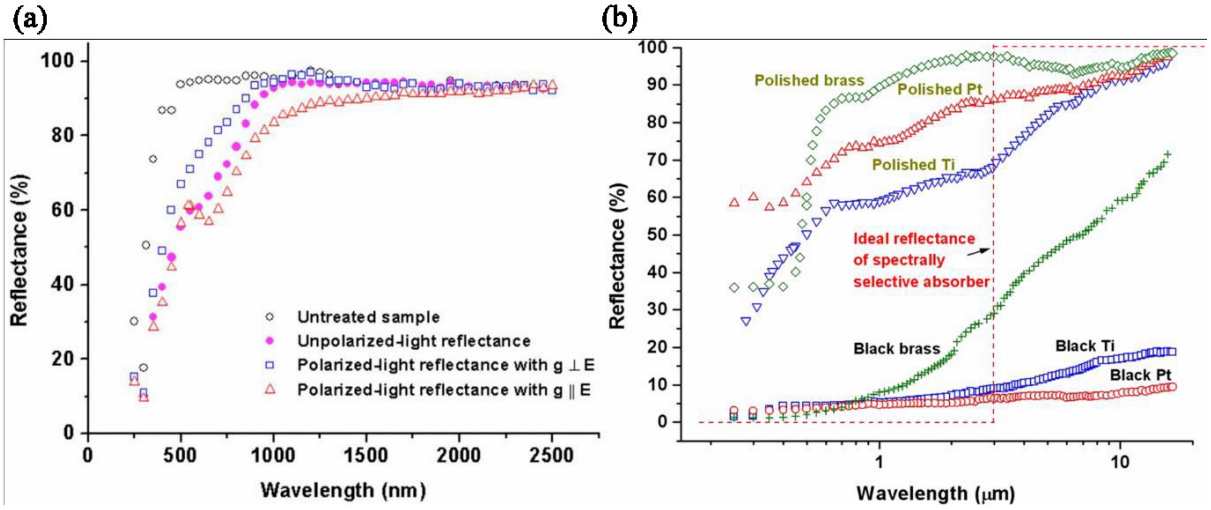

Figure 7: (a) Wavelength dependence of polarized- and unpolarized-light reflectances of the silver sample structured with fs LIPSSs [28] and (b) Spectral reflectance of the black brass, black platinum and black titanium as a function of wavelength. Spectral reflectance of three mechanically polished metals without laser treatment is also shown for a comparison. Dashed line shows the spectral reflectance of an ideal solar absorber [29].

3 EXPERIMENTAL PROCEDURE

In this section, the experimental details regarding the generation and characterisation of the ripples are expounded stepwise.

3.1 EXPERIMENTAL SETUP

A diode pumped Yb:KYW thin disc femtosecond laser system (JenLas® D2.fs, Jenoptik AG, Germany) with a fundamental laser wavelength λ = 1025 nm, a pulse duration τ = 300 fs and laser pulse energies of E_{imp} = 3.5 µJ, 7.5 µJ, 11.0 µJ and 15.5 µJ at pulse repetition frequencies of f_{rep} = 20.833 kHz and 41.667 kHz were used to generate static linearly polarised laser pulses. The pulse repetition frequencies correspond to laser scanning velocities of 0.5 m/s and 1.0 m/s respectively. A plot illustrating the laser pulse energy as a function of the current for our laser setup is provided in figure 8.

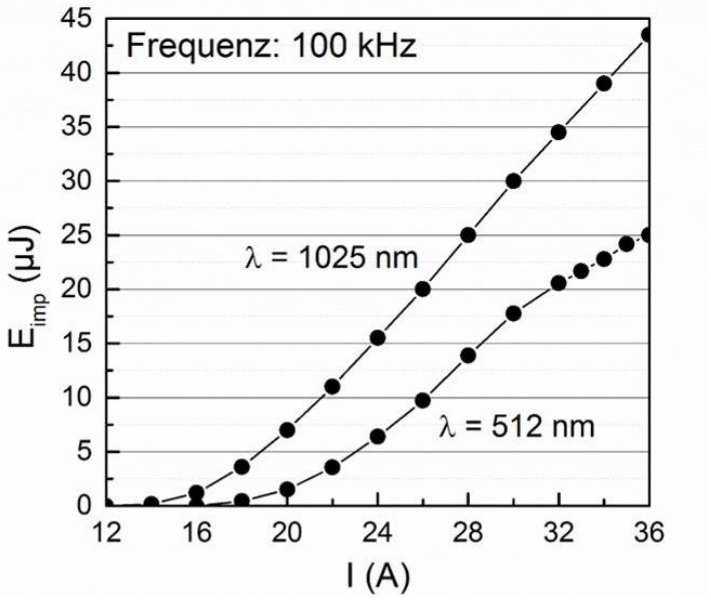

Figure 8: A plot of energy against current for the fundamental and second harmonic wavelength of the diode pumped Yb:KYW thin disc fs-laser system used with a pulse duration of 300 fs and at a frequency of 100 kHz.

Figure 9 shows a picture of the experimental setup utilised in the generation of the LIPSS samples. The pulsed laser beam was ejected via the aperture of the laser head and was directed towards a series of mirrors oriented at some well-defined angles. The laser beam was further guided through a telescope (AK 0142, Jenoptik AG, Germany) that expanded the beam. From the exit point of the telescope, the laser beam passed through two other mirrors which directed the laser beam towards the laser scanner (IntelliSCAN 14, ScanLab, Germany) and finally the beam was focused from the laser scanner through an F-Theta lens (JENar® 1064 nm, Jenoptik,

Germany) to the sample stage. The He-Ne pilot laser in the setup was used to check the alignment of the laser beam on the surface of the substrate material and to also virtually texture the substrate material to check if all parameters were functioning as programmed on the laser scanner software.

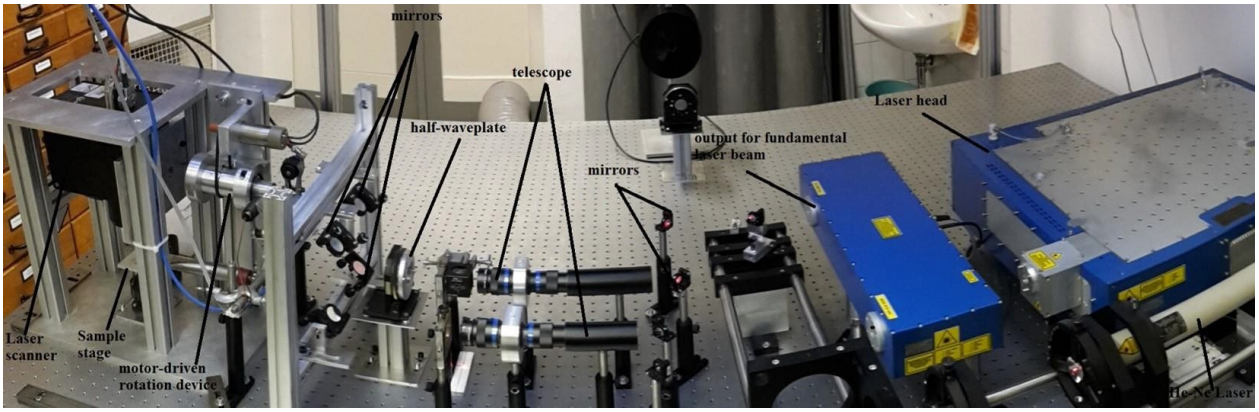

Figure 9: A picture of the fs laser experimental setup utilised in our study for the fabrication of LIPSS.

3.2 SAMPLE PREPARATION

Stainless steel 304 (1.4301; X5CrNi18-10) with dimensions (5×10) mm^2 as well as another one of circular geometry with a diameter of 27 mm were mechanically polished using a polyurethane polishing pad tool and 0.02 µm non-crystallising colloidal silica suspension as polishing agents. Before the laser irradiation of the stainless steel samples, they were ultrasonically cleansed in acetone for 10 minutes and afterwards rinsed in iso-propanol. This step eradicated the dust and/or material debris from the surface of the samples. A non-contact 3D Optical Profiler (CCI HD, Taylor Hobson, England) was utilised to measure the average surface roughness R_a of the polished stainless steel samples. The resulting average roughness was measured to be R_a = 2.7 nm.

3.3 LIPSS GENERATION

LIPSS were generated by irradiating the sample surface at normal incidence and in ambient air. The well-ordered periodic ripples generated with static linearly polarised laser pulses were performed on the (5×10) mm^2 and then later on the 27 mm circular stainless steel samples.

First, with the laser beam directed orthogonal to the stationary sample stage, LIPSS were fabricated on only 5 mm by 5 mm of the total area of the used sample. The experiments were carried out by translating the laser scanner relative to the stationary sample stage with the scanning velocity set to v = 0.5 mm/s.

The direction of the linear polarisation was adjusted parallel ($\alpha = 0°$) relative to v. For these set of experiments, different line spacing of Δx = 25 µm, 20 µm and 10 µm were utilised. An additional laser pulse energy of E_{imp} = 30 µJ was used in this experiment apart from energies of 3.5 µJ and 7.5 µJ. Table 1 shows the matrix of the generated LIPSS samples with the actual laser parameters employed.

Table 1: LIPSS samples generated utilising static linear polarisation parallel to the scanning velocity, $\alpha = 0°$ ($v \parallel E$) with line spacing of 10 µm, 20 µm and 25 µm and for fluences of 0.8 J/cm², 1.7 J/cm² and 6.6 J/cm². The fundamental wavelength λ = 1025 nm of the fs laser was used in these fabrications. A scanning velocity, v = 0.5 mm/s corresponding to some number of laser pulses was utilised.

I = 18 A E = 3.5 µJ F = 0.8 J/cm²	I = 20 A E = 7.5 µJ F = 1.7 J/cm²	I = 30 A E = 30 µJ F = 6.6 J/cm²
Δx = 10 µm	Δx = 10 µm	Δx = 10 µm
Δx = 20 µm	Δx = 20 µm	Δx = 20 µm
Δx = 25 µm	Δx = 25 µm	Δx = 25 µm

In the next LIPSS fabrication with static linear polarised laser pulses, the 27 mm stainless steel sample was used.

In our setup, the sample stage was fixed as well as the sample. However, a computer-programmed laser scanner was utilised in such a manner as to scan through the entire surface of the circularly polished stainless steel substrate material which has a diameter of 27 mm. This enabled us to set and vary some key parameters in the fabrication process such as the diameter and geometry of the sample and the line spacing of the LIPSS.

Furthermore, two marks at 90° interval were made on the 27 mm sample for easy switching and identification of the orientation of LIPSS sample (horizontal or vertical) with respect to the sample holder and the detector. This ensured the precise alignment of the LIPSS for the characterisation using the integrating sphere.

The laser scanner was oriented perpendicular to the sample stage and the sample as well (the incident laser irradiation was polarised horizontally but was focused orthogonal with respect to the sample via a laser scanner with an F-Theta lens of focal length f_L = 100 mm). Laser pulse energies of E_{imp} = 3.5 µJ, 5.5 µJ, 7.5 µJ and 11 µJ were used in this experiment. The typical laser beam diameter focused on the stainless steel sample was measured to be about 24 µm. This resulted in peak fluences of F = 0.8 J/cm^2, 1.7 J/cm^2, 2.4 J/cm^2 and 3.4 J/cm^2. The direction of the linear polarisation was adjusted parallel (α = 0°) relative to v. For these set of experiments, different line spacing of Δx = 20 µm, 15 µm and 10 µm were used. Table 2 shows the matrix of the generated samples with the actual laser parameters employed.

Air pressure was used to help protect the lens of the laser scanner and to also help wash off some plasma, steam and dust that were also generated on the polished stainless steel sample because of the laser structuring or LIPSS generation. With all the parameters set, the laser was therefore initiated to begin the LIPSS fabrication process.

Table 2: Displaying LIPSS samples generated utilising scanning velocities of v = 1 m/s and v = 0.5 m/s corresponding to number of laser pulses N = 2.4 and N = 4.8 respectively. Static linear polarisation parallel to the scanning velocity, α = 0° ($v \parallel E$) was utilised. The line spacing was 10 µm, 15 µm and 20 µm for fluences of 0.8 J/cm^2, 1.7 J/cm^2, 2.4 J/cm^2 and 3.4 J/cm^2. The fundamental wavelength λ = 1025 nm of the fs laser was used in these fabrications.

	I = 18 A E = 3.5 µJ F = 0.8 J/cm^2	I = 20 A E = 7.5 µJ F = 1.7 J/cm^2	I = 22 A E = 11 µJ F = 2.4J/cm^2	I = 24 A E = 15.5 µJ F = 3.4 J/cm^2
v = 0.5 m/s N = 4.8	Δx = 10 µm Δx = 15 µm Δx = 20 µm	Δx = 10 µm Δx = 15 µm Δx = 20 µm	Δx = 10 µm Δx = 15 µm Δx = 20 µm	Δx = 10 µm Δx = 15 µm Δx = 20 µm
v = 1. 0 m/s N = 2.4	Δx = 10 µm Δx = 15 µm Δx = 20 µm	Δx = 10 µm Δx = 15 µm Δx = 20 µm	Δx = 10 µm Δx = 15 µm Δx = 20 µm	Δx = 10 µm Δx = 15 µm Δx = 20 µm

3.4 CHARACTERISATION OF LIPSS

The laser irradiated sample surfaces were cleansed in acetone and immediately rinsed in iso-propanol and dried using some air pressure so as so to remove the dust or material debris off the surface of the samples. The morphology of the samples was subsequently characterised using scanning electron microscopy SEM. The stainless steel samples were examined with SEM (S440i, Leica, Germany) at an accelerating voltage of 20 kV and at a working distance of 5 mm using the secondary electron detector. From the SEM micrographs, fast Fourier transforms FFTs were performed using Gwyddion (open source) software to evaluate the period of the LIPSS.

3.5 DIFFRACTION PATTERN MEASUREMENT OF LIPSS

Following the LIPSS fabrication on the (5×10) mm^2 stainless steel substrates, the wavelength dependent intensity measurements were performed. To do this investigation of the colour change effect, the stainless steel LIPSS samples were utilised as diffraction gratings.

Figure 10 illustrates the detailed schematic diagram of the setup employed for these measurements. The setup comprises an unpolarised Xenon arc lamp (Power Arc™, Optical Building Blocks, USA) which served as our white light source and functions at a wavelength range between 200 nm and 1100 nm, a fibre cable to couple and guides the light beam to the other components of the setup. The light source was expanded to obtain the optimal focal spot size. This also enabled the light beam to be collimated and helped to obtain the minimum beam divergence possible as well. These were achieved by means of a telescope which consists of two lenses. From the telescope, the light beam passed through an aperture which further focused the beam of light in the defined region. From there, the beam of light was directed unto the LIPSS sample in its holder (with the incident light beam oriented orthogonal to the LIPSS sample). The detector in our case was positioned in such a way as to detect almost all the diffracted or scattered light incident on the LIPSS sample. The signal from the detector was then fed into the spectrophotometer (Spectra Suite, Ocean Optics, USA) and analysed with the Spectra Suite software. The integration time used was 15 ms. The schematic diagram setup displayed in figure 10 further elucidates the description and provides more details for comprehension.

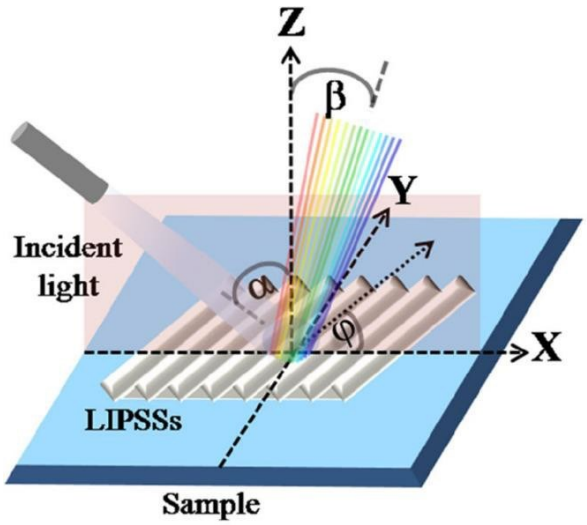

Figure 10: A schematic diagram of the experimental setup used in the investigation of the colour change exhibited by our LIPSS samples. The LIPSS sample were fabricated with a laser *E*-field polarisation, α = 0° [12].

The LIPSS sample was slightly shifted by an angle of about 1° such that the whole white light source is reflected from the polished stainless steel LIPSS sample unto the detector. A wavelength range from 350 nm to 1000 nm was utilised in our measurements since the Xenon arc lamp functions best in the mentioned range. Furthermore, a division of each measured spectra at the various diffraction angles from 25° to 70° by the reference spectrum was performed in order to obtain new spectra which excludes the reference.

To optimise and precisely get the required position of the detector from the LIPSS sample, the distance of the detector to the LIPSS sample was varied. When the detector was positioned relatively far away from the LIPSS sample, a clear and visibly-wide spectrum was displayed on the computer. On the contrary, when the detector was positioned relatively near the LIPSS sample, an unclear and crowded spectrum was displayed on the computer. It was thus inferred that the position of the detector relatively far away from the LIPSS sample was preferred.

The detector position with respect to the LIPSS sample (diffraction angle) was varied from 25° to 70° in steps of 5° so as to observe and measure the diffracted colour (wavelength) and its corresponding intensity for each change in the viewing angle. A schematic diagram to illustrate the diffraction grating behaviour of the LIPSS is provided in figure 11.

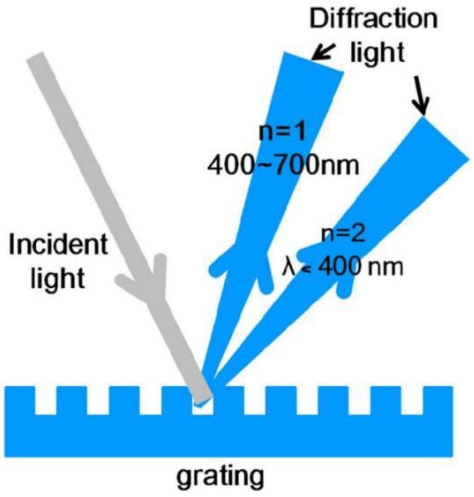

Figure 11: The schematic diagram for the diffraction grating behaviour exhibited by the LIPSS sample [12].

3.6 REFLECTANCE MEASUREMENT WITH AN INTEGRATING SPHERE

To get further insight into the optical behaviour (reflectance) of the irradiated stainless steel substrate materials, the integrating sphere with UV-Vis-NIR spectrophotometer was employed. With this instrument, the total as well as diffuse reflectance spectra for both the unirradiated and the irradiated stainless steel substrate materials were measured and analysed accordingly. The specular reflectance data were obtained by subtracting the diffuse reflectance data from the total reflectance.

The experiments were performed using the integrating sphere (ISR-3100, Shimadzu, Japan) that employs some UV-Vis-NIR spectrophotometer in the range of 240 nm – 2600 nm as the measuring device for the reflectance investigations. The measurements with the integrating sphere were performed under the following parameters: for wavelength range of 240 nm – 800 nm (for the Photomultiplier detector), wavelength steps of 1 nm and a slit width of 5 nm was used. However, for the wavelength range of 800 nm - 2600 nm (for the PbS cell detector), wavelength steps of 1 nm and a slit width of 20 nm was used. For this reason, the detector switching point was around 800 nm when the Photomultiplier (PMT) detector was changed to the PbS cell detector. The samples used in this investigation were the static linearly polarised LIPSS fabricated on the circular stainless steel with a diameter 27 mm.

Figure 12 displays a picture of the integrating sphere used in our measurements. For the measurements with the integrating sphere, a beam of unpolarised monochromatic light source from the spectrophotometer was focused onto the LIPSS sample. The sample was placed such that it lied on a tangent to the inside radius of the integrating sphere. The reflected sample was then collected by the sphere, which offered a 180° field of collection. The detector(s) lied at another location on the inside tangent of the sphere and collected the total and diffuse reflected radiation.

The measurements were conducted at fixed incident angles of 8° and 0° for total and diffuse reflectance measurements respectively. The LIPSS samples were oriented either horizontal or vertical with respect to the sample holder as well as with the white light illuminating source and the detector.

Total reflectance measurements were performed when the incident beam was driven unto the LIPSS sample at an incident inverse angle of 8°. The light beam then impinged on a mirror placed at the defined angle and from there, the beam was driven straight towards the LIPSS

sample. On the contrary, for diffuse reflectance measurements, the measurements were done when the incident light beam was driven directly unto the LIPSS sample at an angle of 0°.

In our measurements, our reference reflectance spectrum which is the $BaSO_4$ standard, the coating of the integrating sphere utilised in our measurements, was first measured. We then measured the reflectance spectrum of the unirradiated polished stainless steel against $BaSO_4$ standard. The measurement was done first in the inverse or total reflectance mode and then later in the diffuse reflectance mode. From this we obtained the spectrum of only the unirradiated polished stainless steel sample. Afterwards, the LIPSS fabricated samples were also measured against the $BaSO_4$ standard for both total and diffuse reflectance. From this, the total and diffuse reflectance spectra for only our LIPSS fabricated samples were obtained.

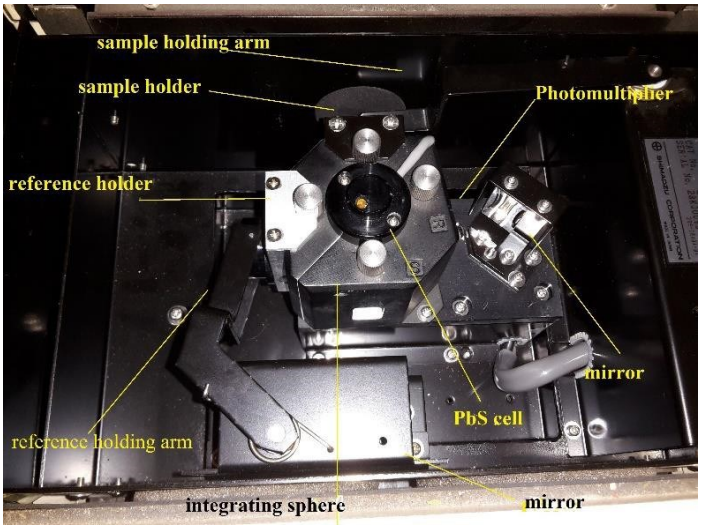

Figure 12: A labelled internal view of the integrating sphere.

Following the data obtained from the total and diffuse reflectance measurements as well as the specular reflectance data, graphs corresponding to the three reflectance measurements were plotted and the necessary comparisons and discussions were then made.

4 RESULTS

4.1 STRUCTURAL CHARACTERISATION OF LIPSS

The structural and morphological features of the LIPSS samples fabricated with varying laser parameters such as fluence, line spacing, number of laser pulses or scanning velocity characterised utilising the scanning electron microscope are hereby presented.

Figure 13 shows SEM micrographs of LIPSS generated on polished stainless steel samples. The (5×10) mm^2 stainless steel samples were irradiated utilising a scanning velocity v = 0.5 mm/s, f_{rep} = 250 Hz and varying laser fluences of F = 0.8 J/cm^2, 1.7 J/cm^2 and 6.6 J/cm^2 and also with static linear polarisation parallel to v ($\alpha = 0°$). Figure 13 sample (0.8 J/cm^2, 25 µm), sample (1.7 J/cm^2, 25 µm) and sample (6.6 J/cm^2, 25 µm) show the SEM images with the E-field vector oriented perpendicular to the orientation of the LIPSS and all with line spacing of 25 µm. The fluence is the distinguishing feature between these three figures. Figure 13 (f) with a fluence of 6.6 J/cm^2 possesses higher visibility and width than the other fluences of 1.7 J/cm^2 (figure 13 (d)) and 0.8 J/cm^2 (figure 13 (b)) respectively. Similar results pertaining to high visibility at the highest fluence of 6.6 J/cm^2 was observed on the SEM images for LIPSS fabricated with a line spacing of 10 µm (figure 13 (e)) compared to the SEM images for figures 13 (a) and (c) corresponding to fluences of 0.8 J/cm^2 and 1.7 J/cm^2 respectively.

The period of the LIPSS increased from 875 nm to 903 nm with increasing fluence at a line spacing of 10 µm. At a line spacing of 25 µm, the period of the LIPSS increased from 910 nm to 960 nm with increasing fluence. Table 3 provides further information on the periodicity of LIPSS evaluated using open source software Gwyddion. The increase of the periodicity with increasing fluence is also evident when figures 13 (a), (c) and (e) with varying fluences but all with the same line spacing of 10 µm are inspected closely. These same results exist for figures 13 (b), (d) and (f) with varying fluences but all with a line spacing of 25 µm.

With increasing line spacing, the periodicity of LIPSS increased from 875 nm to 910 nm at a fluence of 0.8 J/cm^2. Similarly, the LIPSS period increased with increasing line spacing from 903 nm to 960 nm at a fluence of 6.6 J/cm^2. A critical look at SEM micrographs for figures 13 (a) and (b) display LIPSS fabricated using the same fluence of 0.8 J/cm^2 but at varying line spacing of 10 µm and 25 µm respectively. These further confirm that the period of the LIPSS sample fabricated with a line spacing of 25 µm possesses the largest period. Table 3 shows the evaluated periods of the LIPSS.

From the SEM images, we again observed that the LIPSS generated with a line spacing of 10 µm exhibit some sub-LIPSS section separations for some fluence values. These sub-LIPSS sections are more pronounced especially at the lowest fluence (0.8 J/cm^2 in this case) as can be observed in figure 13 (a).

The periodicity of LIPSS again increased with increasing line spacing from 820 nm to 900 nm at a fluence of 0.8 J/cm^2. At a fluence of 3.4 J/cm^2, the LIPSS period increased with increasing line spacing from 859 nm to 960 nm. The periodicity of the LIPSS is shown in table 4.

The LIPSS generated over the entire designated area are continuous regardless of the line spacing or other differing laser parameters used. The energy (intensity) of the laser pulse is significantly higher in the centre of the irradiated area as a result of the Gaussian beam profile of the used laser.

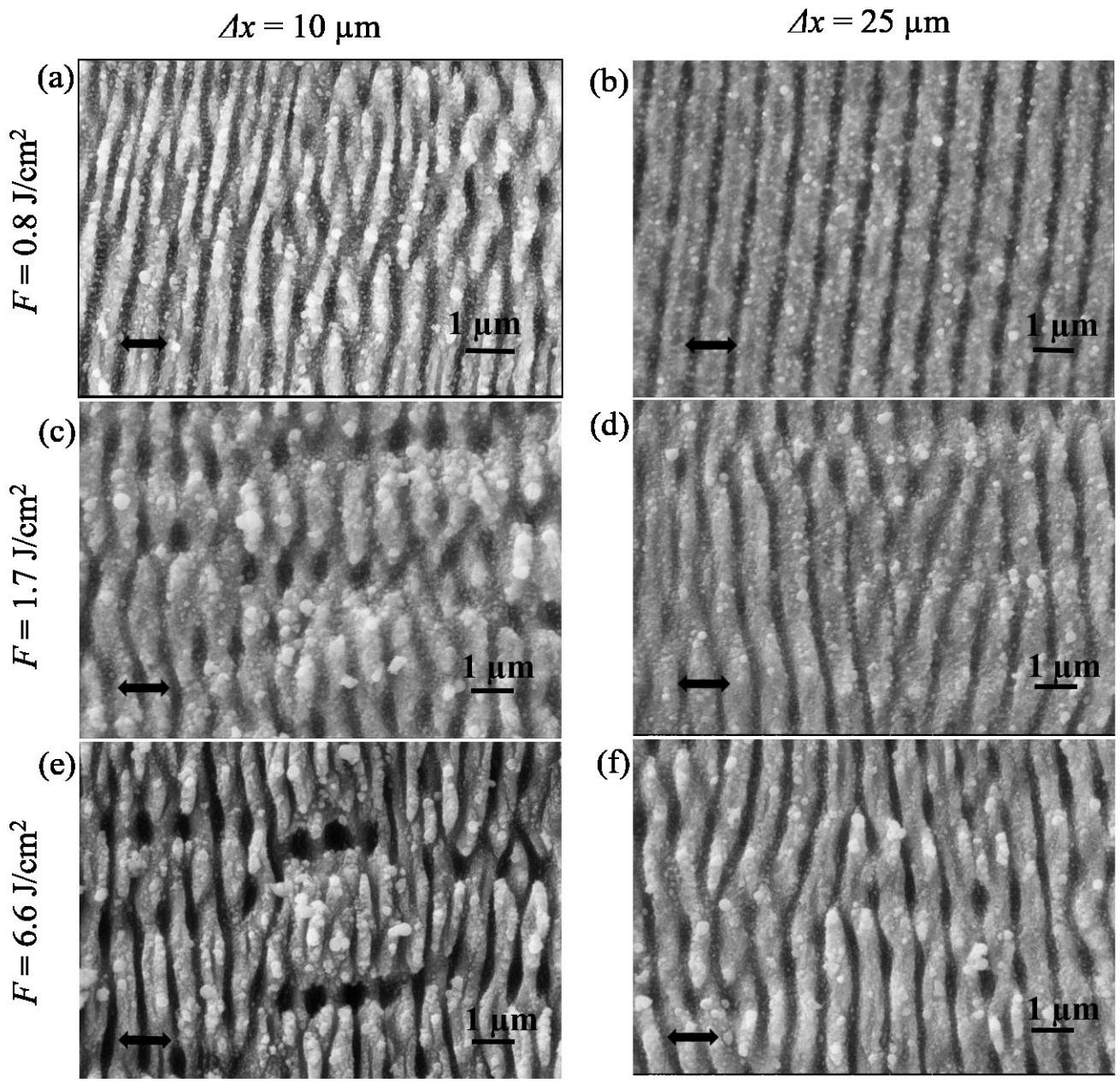

Figure 13: SEM micrographs of the stainless steel LIPSS samples generated using static linear polarisation at a direction of $\alpha = 0°$ ($v \parallel E$) and at a scanning velocity of $v = 0.5$ mm/s. The SEM micrographs were obtained at a working distance of 5mm, voltage of 20 kV. The black double-headed arrows indicate the direction of the incident laser polarisation. (a) and (b) are at a fluence of 0.8 J/cm^2, (c) and (d) are with a fluence of 1.7 J/cm^2, (e) and (f) are with a fluence of 6.6 J/cm^2. Line spacing of $\Delta x = 10$ µm and $\Delta x = 25$ µm were used in the fabrication of the LIPSS.

Table 3: The experimental mean period for the stainless steel samples. The periods were obtained using Gwyddion software and a trivial manual evaluation.

Sample	Period [nm]
0.8 J/cm^2, 25 µm	910
1.7 J/cm^2, 25 µm	940
6.6 J/cm^2, 25 µm	960
0.8 J/cm^2, 20 µm	908
1.7 J/cm^2, 20 µm	922
6.6 J/cm^2, 20 µm	930
0.8 J/cm^2, 10 µm	875
1.7 J/cm^2, 10 µm	895
6.6 J/cm^2, 10 µm	903

Performing an optical microscopic as well as a SEM investigation on the fabricated samples after LIPSS fabrication revealed the detailed geometry of the LIPSS from the laser spots. The samples investigated here were irradiated in scanning mode with different laser fluences and different number of laser pulses or scanning velocities.

For these set of fabricated LIPSS, there was a slight tilt (about 6°) in the direction of the laser scanner towards the sample and this is visible in all the SEM micrographs in figures 14 and 15. This shift might have been occasioned by a slight tilt in the polarisation of the laser scanner.

Conducting a preliminary SEM investigation, a laser fluence of 2.0 J/cm^2 and different number of laser pulses or scanning velocities were utilised. It was observed that using a laser pulse N = 1.00 (v = 3.00 m/s), LIPSS with continuous series of circles or ring shapes (but with no visible overlaps of the ring shapes) were generated (see figure 14 (a)). This was actually expected as each laser spot should produce some ring-shaped geometry. In figure 14 (b), there was an observation of some little overlap between adjacent laser spots at N = 1.10 (v = 2.25 m/s). Generally as N was increased from N = 1.10 to N = 1.60 and beyond, we observed an appearance of more pronounced overlaps between adjacent ring shapes in the form of a

perturbation. As the scanning velocity v increased, the number of laser pulses per spot, N decreased according to the relation:

$$N = {}^{2wf_{rep}}/_{v} \quad (2)$$

Where v is the scanning velocity, w is the laser beam diameter, and f_{rep} is the repetition rate of the laser.

Decreasing N therefore implied the creation of larger distinction (gaps) between the individual ring-shaped spots observed in the fabrication of LIPSS. At N = 1.60 pulses per spot (v = 1.50 m/s), the overlap between adjacent ring-shaped structures increased, and as such a more enhanced morphological feature was seen in figure 14 (c) in comparison to N = 1.00 shown in figure 14 (a). For N = 2.40 pulses per spot (v = 1.00 m/s) corresponding to figure 14 (e), the overlaps intensified and as a result, the ring-shaped features were almost invisible – visible LIPSS with continuous lines were observed in this case. Figure 14 (k) represents, N = 4.80 pulses per spot (v = 0.50 m/s) and for this, brighter and straight continuous lines were observed – ring shapes were completely absent due to the dominance of the overlaps and the straight periodic patterns. For N = 7.27 pulses per spot (v = 0.33 m/s), the depth and width of the overlap further increased and the visibility of the straight continuous patterns were enhanced. N = 9.60 pulses per spot (v = 0.25 m/s) showed a more pronounced visible LIPSS. Finally, for N = 12 pulses per spot (v = 0.20 m/s) LIPSS that overlap so closely such that the pattern could be said to exhibit ideal grating-like characteristics was observed. A perfect grating was thus observed with increasing number of pulses (decreasing scanning velocity). Figure 14 illustrates the evolution of the morphological feature changes that occurred on the LIPSS as the scanning velocity (number of laser pulses) was varied at a constant fluence. The other scanning velocities from 0.33 m/s to 0.20 m/s are however, not shown because they exhibited similar features like the structures with v = 0.50 m/s but with more perfect LIPSS.

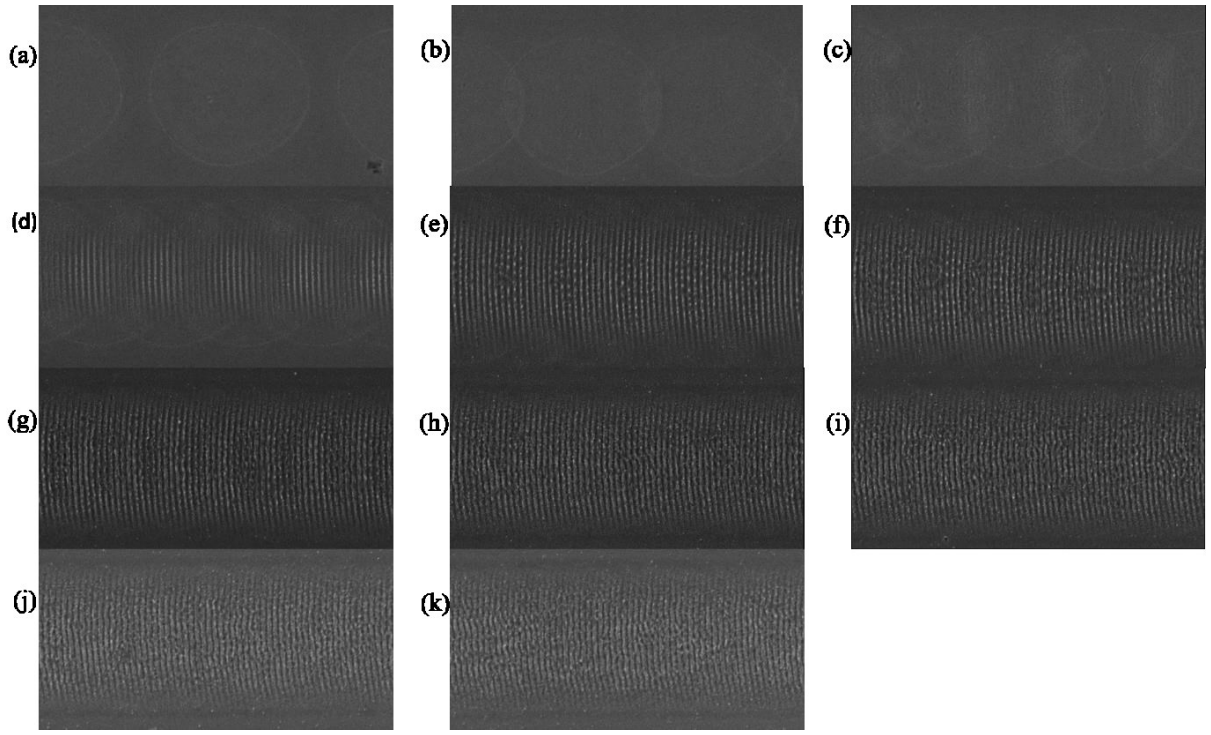

Figure 14: SEM micrographs displaying the investigation of LIPSS morphological evolution with varying scanning velocity (number of pulse irradiation). LIPSS were fabricated at a fluence of F = 2.0 J/cm^2. The various scanning velocities utilised were: (a) 3.00 m/s (b) 2.25 m/s (c) 1.50 m/s (d) 1.20 m/s (e) 1.00 m/s (f) 0.86 m/s (g) 0.75 m/s (h) 0.66 m/s (i) 0.60 m/s (j) 0.55 m/s and (k) 0.50 m/s.

A comparison between the LIPSS formed using v = 1 m/s and v = 0.5 m/s can be made for figure 15 (a) and (e) as well as for figure 15 (b) and (f). It was clearly evident that SEM images for the LIPSS with low scanning velocity appeared more visible (larger overlaps) than the LIPSS with high scanning velocity. The square-like spots that appeared in figure 15 (a) were entirely absent in figure 15 (e). Figure 15 (f) showed a SEM image with almost no gaps between the adjacent straight line patterns as compared with figure 15 (b) which showed very large gaps with very small overlaps between the other straight line patterns. The degree of the visibility of the surface morphological features seen in figure 15 (e) was undoubtedly higher than that observed for figure 15 (f). This was likewise higher than those observed in figures 15 (a) and (b). Figure 15 (e) showed an entirely continuous LIPSS with large overlaps between the spots and hence could be seen to be crowding together in the form of one huge spot (nearing an ideal grating-like behaviour). The converse is true in figure 15 (f); there was still evidence of some clearly unirradiated spots or regions in its SEM image.

At a fluence of 3.4 J/cm^2, figures 15 (c) and (d) were fabricated at v = 1 m/s. On the other hand, figures 15 (g) and (h) were fabricated at v = 0.5 m/s. At this fluence too, it was obvious that the LIPSS generated with the low scanning velocity portrayed LIPSS with the highest visibility for the different line spacing as is evident in the SEM micrographs.

A closer look at figure 15 (c) revealed some few unirradiated spots whereas in figure 15 (g), the entire surface was covered with LIPSS. A similar observation can be made for figure 15 (d) and figure 15 (h). Figure 15 (d) showed even more non-ablated spots when compared with figure 15 (c). Likewise figure 15 (g) showed a completely irradiated LIPSS in comparison to figure 15 (h).

The periodicity of LIPSS decreased from 960 nm to 820 nm for increasing number of pulses from $N = 2.4$ to $N = 4.8$ but increased from 820 nm to 960 nm for increasing scanning velocity from $v = 0.5$ m/s to $v = 1$ m/s. The decrease in periodicity occurred with decreasing fluence and vice versa.

The SEM micrographs shown in figures 15 (a) and (b) correspond to fluence of 0.8 J/cm^2 but at a line spacing of 10 µm and 20 µm respectively. A more visible LIPSS is of course observed for the lower line spacing of 10 µm. Larger overlaps between the ring-shaped structures are also observed for the LIPSS with a line spacing of 10 µm. The inset of figure 15 (a) shows a SEM image with larger overlaps. The inset of figure 15 (b) however shows just little overlaps between the ring-shaped spots. With increasing line spacing, the periodicity of LIPSS increases from 820 nm to 920 nm and from 879 nm to 960 nm at a scanning velocity of $v = 0.5$ m/s and $v = 1$ m/s respectively. Table 4 provides further details on the periodicity of the LIPSS.

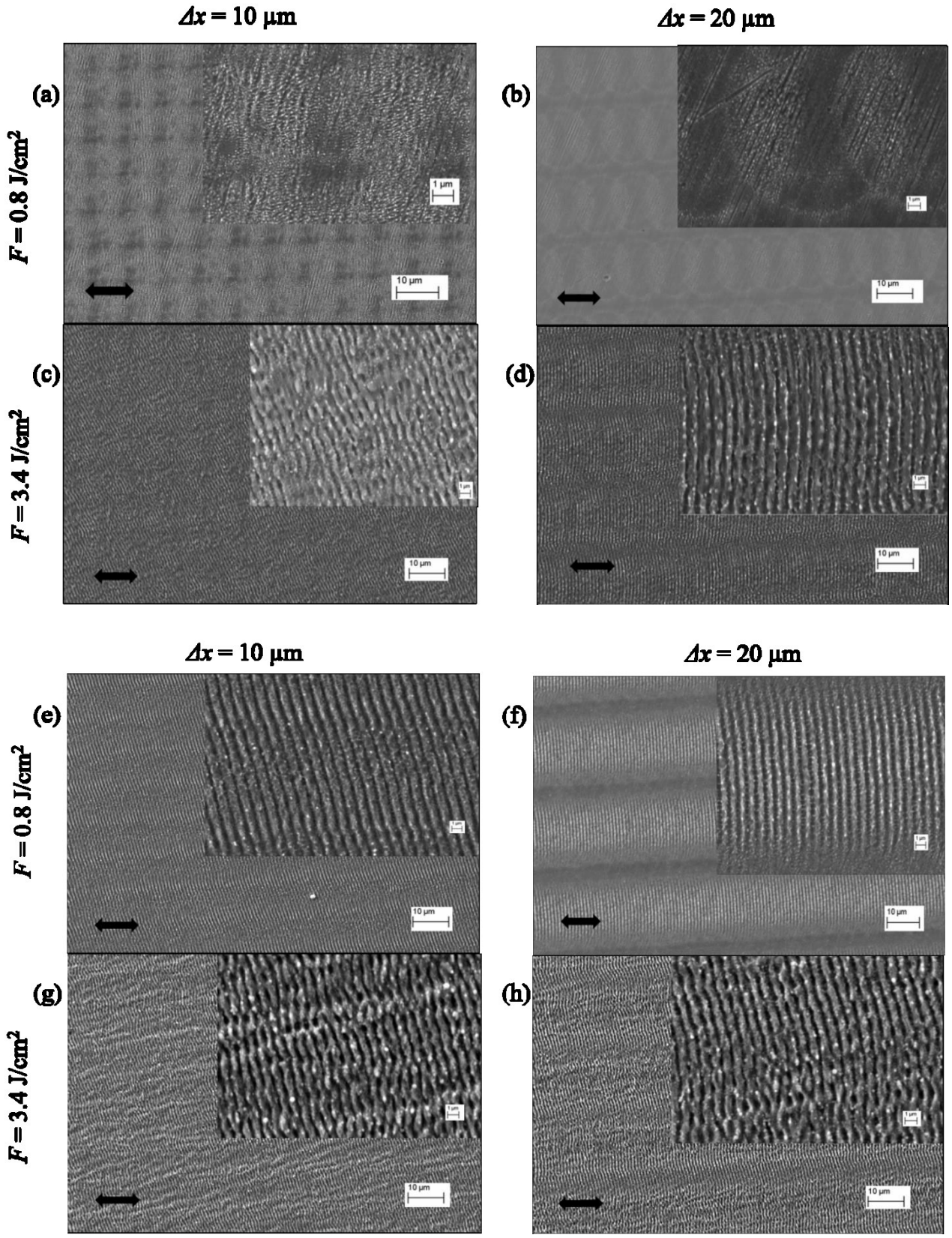

Figure 15: Morphological evolution of LIPSS on stainless steel substrate induced by fs laser with varied fluences of $F = 0.8$ J/cm² and $F = 3.4$ J/cm². (a) – (d) are fabricated with a scanning velocity of $v = 1$ m/s and (e) – (h) are fabricated with a scanning velocity of $v = 0.5$ m/s. The double-edged arrow indicates the direction of the E-field vector $\alpha = 0°$ ($v \parallel E$). The inlets are SEM micrographs at a much higher magnification.

Table 4: Average period for stainless steel LIPSS samples fabricated with scanning velocities of v = 1 m/s and v = 0.5 m/s. The periods were obtained using Gwyddion software and a trivial manual evaluation.

Sample at v = 1 m/s	Period [nm]	Sample at v = 0.5 m/s	Period [nm]
0.8 J/cm^2, 20 µm	900	0.8 J/cm^2, 20 µm	884
1.7 J/cm^2, 20 µm	920	1.7 J/cm^2, 20 µm	912
2.4 J/cm^2, 20 µm	935	2.4 J/cm^2, 20 µm	915
3.4 J/cm^2, 20 µm	960	3.4 J/cm^2, 20 µm	920
0.8 J/cm^2, 15 µm	883	0.8 J/cm^2, 15 µm	850
1.7 J/cm^2, 15 µm	903	1.7 J/cm^2, 15 µm	884
2.4 J/cm^2, 15 µm	933	2.4 J/cm^2, 15 µm	902
3.4 J/cm^2, 15 µm	941	3.4 J/cm^2, 15 µm	930
0.8 J/cm^2, 10 µm	879	0.8 J/cm^2, 10 µm	820
1.7 J/cm^2, 10 µm	884	1.7 J/cm^2, 10 µm	830
2.4 J/cm^2, 10 µm	920	2.4 J/cm^2, 10 µm	850
3.4 J/cm^2, 10 µm	925	3.4 J/cm^2, 10 µm	859

4.2 OPTICAL PROPERTIES OF LIPSS

4.2.1 COLOURATION

As can be observed from figures 16 and 17, the colours covered the entire visible spectrum (400 nm to 750 nm). Different colours, including blue (λ = 450 – 495 nm), green (λ = 495 – 570 nm), orange (λ = 490 – 620 nm) and some yellow (λ = 570 – 590 nm) in the transition region between green and orange, at different viewing angles by the naked eyes and mainly with the detector in our case were evident. It was further observed that the wavelength gradually shifted from the blue colour to red and even to the infra-red (IR) region when the angle of the detector with respect to the LIPSS substrate was increased from 25° to 70°. A wavelength in the IR spectra region (close to the period of the LIPSS, Λ = 875 - 960 nm) was observed at higher angles of the detector (60° to 70° in our case). This was noticed in the plots shown in figures 16 (a) – (g) and figure 17 for varying fluences and line spacing.

Furthermore, the intensity values of the first diffraction order peaks in sample (0.8 J/cm^2, 25 μm) were seen to be higher than in sample (1.7 J/cm^2, 25 μm) and sample (6.6 J/cm^2, 25 μm) as a result of the low fluence in sample (0.8 J/cm^2, 25 μm). Sample (0.8 J/cm^2, 25 μm) and sample (1.7 J/cm^2, 25 μm) did not vary that much in intensity since their respective fluence of 0.8 J/cm^2 and 1.7 J/cm^2 are very close. The intensity value in sample (6.6 J/cm^2, 25 μm) was observed to be very low but covered a broad region because of the high fluence of F = 6.6 J/cm^2 (highly blackened LIPSS) utilised in its fabrication. Hence, almost all the intensity from the white light source (Xenon arc lamp) would subsequently be absorbed by the sample (6.6 J/cm^2, 25 μm) as illustrated in figure 16 (g). From the graphs, we therefore observe from sample (0.8 J/cm^2, 25 μm), sample (1.7 J/cm^2, 25 μm) and sample (6.6 J/cm^2, 25 μm), a continuous decrease in intensity but an increase in the peak width (FWHM) for increasing fluence at fixed line spacing. In general, it was observed that the intensity of the first diffraction order peaks for increasing wavelength decreased as the line spacing was decreased. These were more evident in figures 16 (a), (b) and (c) representing a fluence of F = 0.8 J/cm^2 and figures 16 (g), (h) and (i) representing a fluence of F = 6.6 J/cm^2.

There appeared some second harmonic wavelength (that is an appearance of a second diffraction order peak which occurs at a wavelength which is half of the first diffraction order peak) for sample (0.8 J/cm^2, 25 μm) shown in figure 16 (a). This second harmonic wavelength (second diffraction order peak) was also evident in sample (0.8 J/cm^2, 20 μm,) shown in figure 16 (b) but was not visible in sample (0.8 J/cm^2, 10 μm) shown in figure 16 (c) which are all

with similar fabricating parameters of F = 0.8 J/cm^2 but with decreasing line spacing. The second diffraction order occurred in our case at higher diffraction angles of β = 55° to 70° for sample (0.8 J/cm^2, 20μm) see figure 16 (b) and sample (0.8 J/cm^2, 25 μm) see figure 16 (a). From figures 16 (a), (b) and (c), the plots for fluence of 0.8 J/cm^2 but at decreasing line spacing from 25 μm to 10 μm are illustrated. The ratio of the intensity of the first diffraction order peaks to the second diffraction order peaks for increasing wavelength decreased with decreasing line spacing.

All the samples herein investigated from sample (0.8 J/cm^2, 25 μm) through to sample (6.6 J/cm^2, 10 μm) were all fabricated with the same polarisation direction α = 0°. It could be agreed that there was always some specific wavelength peak visible except for sample (6.6 J/cm^2, 25 μm), sample (6.6 J/cm^2, 20 μm) and sample (6.6 J/cm^2, 10 μm) which were all fabricated with a fluence F = 6.6 J/cm^2. Hence the fluence of F = 6.6 J/cm^2 is excluded in figure 17 because the LIPSS were so deep and thick and as a result most of the incident light intensity would subsequently be absorbed leaving merely a low but very broad (not so pronounced) intensity peak as are illustrated in figures 16 (g), (h) and (i).

Figures 16 (a), (d) and (g), illustrate the plots for LIPSS fabricated at a line spacing of 25 μm but at varying fluences of 0.8 J/cm^2, 1.7 J/cm^2 and 6.6 J/cm^2 respectively. Perfect LIPSS (grating structures) were generated at this line spacing since there appeared diffraction peaks for varying diffraction angles for increasing fluences. These diffraction peaks however, diminished as the fluence increased from 0.8 J/cm^2 to 6.6 J/cm^2. Furthermore, a continuous decrease in intensity with increasing diffraction angles was noticed. Similar observations were noticed for figures 16 (b), (e) and (h) at a line spacing of 20 μm and figures 16 (c) and (f) at a line spacing of 10 μm. In figure 16 (i), there was no observable diffraction order peak since the entire light beam incident on the LIPSS was absorbed.

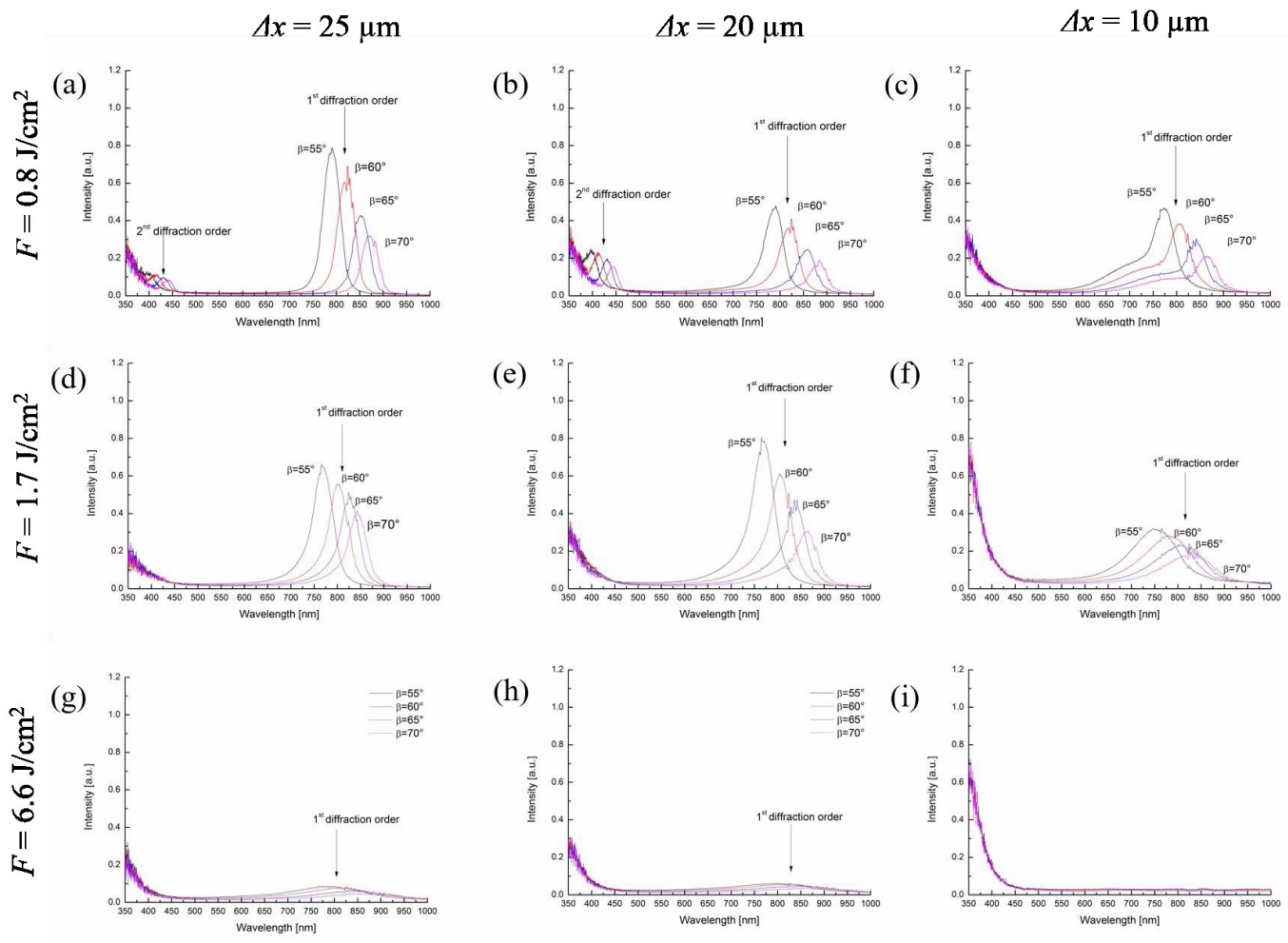

Figure 16: Plots of intensity against wavelength for several LIPSS samples with the same laser polarisation α=0° ($v \parallel E$), and at different laser fluences of F= 0.8 J/cm², F= 1.7 J/cm² and F= 6.6 J/cm². The line spacing for the samples are also different with (a), (d) and (g) with Δx=25 µm (b), (e) and (h) with Δx=20 µm and (c), (f) and (i) with Δx=10 µm. The different diffraction angles used are β = 55°, 60°, 65° and 70°. The plot also illustrates the peak of the diffraction patterns for both the first and the second diffraction orders.

Figures 17 (a) and (b) display an almost linear dependence of wavelength on the diffraction angle for varying line spacing of 25 µm, 20 µm and 10 µm at fluences of 0.8 J/cm² and 1.7 J/cm². The figures further show that the wavelength increased as the diffraction angles were increased. Comparatively, the largest line spacing of 25 µm produced the highest wavelength value for increasing diffraction angles in both plots (with two different fluences) with the smallest line spacing always yielding the lowest wavelength for increasing diffraction angles.

It could also be observed that the plot for the lower fluence of 0.8 J/cm² see figure 17 (a) displayed relatively higher wavelength values for increasing diffraction angles and for increasing line spacing when compared with the plot at a fluence of 1.7 J/cm² (figure 17 (b)).

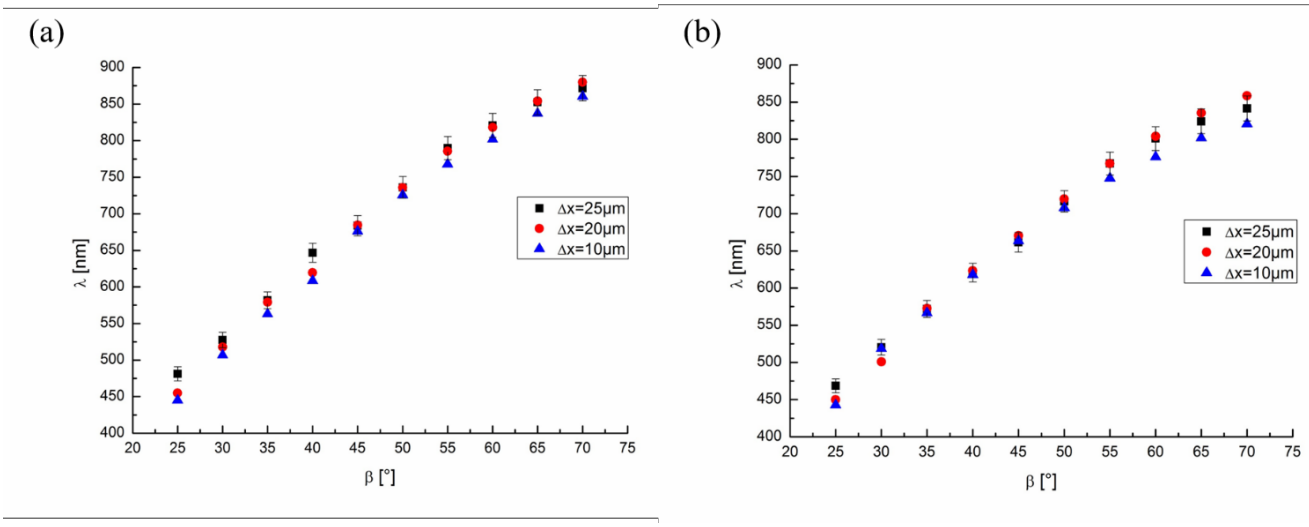

Figure 17: Plots of wavelength λ against diffraction angle β for different LIPSS samples with the same laser polarisation α=0° ($v \parallel E$), and at a laser fluence of (a) F= 0.8 J/cm^2 and (b) F= 1.7 J/cm^2. The line spacing Δx for the samples are however different; 25 µm for square, 20 µm for circle and 10 µm for triangle legends respectively.

4.2.2 REFLECTANCE

Following the measurements of LIPSS utilising the integrating sphere, total, diffuse and specular reflectance data were obtained. The plots in figures 18 and 19 illustrate the comparison between the various reflectance measurements and some laser parameters employed in the LIPSS fabrication process. The detector switching point (from PMT to PbS detector) is illustrated with a grey rectangle. The switching occurs at the wavelength range of 800 – 840 nm.

Figures 18 (a) – (i) display the total, diffuse and specular reflectance spectra for line spacing of 10 µm, 15 µm and 20 µm, scanning velocity of 0.5 m/s and at laser fluences of 0.8 J/cm^2 to 3.4 J/cm^2. The figures in general depict low total and specular reflectance in the UV, but increase in the Vis and go even higher in the NIR. The total reflectance values at a wavelength of 900 nm for fluences of 0.8 J/cm^2, 1.7 J/cm^2, 2.4 J/cm^2 and 3.4 J/cm^2 were 0.43, 0.36, 0.32 and 0.29 respectively as shown in figure 18 (a). There was therefore a general observation of a decrease in the total reflectance spectra as the fluence was increased. The unirradiated sample therefore produced the highest total reflectance spectrum followed closely by the sample irradiated with the lowest fluence of 0.8 J/cm^2 in our experiment. Figures 18 (a), (d) and (g) further elucidate this assertion. The results also portrayed the fact that as the laser fluence was increased for the same scanning velocity v = 0.5 m/s but at different line spacing of 10 µm, 15 µm and 20 µm respectively, the total reflectance spectra kept increasing. The total

reflectance was lowest for the smallest line spacing of 10 µm and highest for the largest line spacing of 20 µm.

Additionally, there was observation of some valley-like features around wavelengths values of 580 nm and 1150 nm. These features appeared for almost all laser fluences and were mainly visible at a fluence of 0.8 J/cm^2 for increasing line spacing. At fluences of 1.7 J/cm^2 and 2.4 J/cm^2, the features were less pronounced at a line spacing of 10 µm but became visible at line spacing of 15 µm and 20 µm. The features were however, almost absent at a fluence of 3.4 J/cm^2. The valley-like features were absent in the unirradiated sample spectra as well. Also, the valley-like features appeared deeper at larger line spacing of 20 µm and were of course shallow at a small line spacing of 10 µm.

The unirradiated stainless steel sample showed the lowest diffuse reflectance spectra for the entire wavelength range considered. This was followed by the sample irradiated with the lowest fluence of 0.8 J/cm^2. At a wavelength of 900 nm, the lowest fluence showed a diffuse reflectance value of 0.22. For fluences of 1.7 J/cm^2 and 2.4 J/cm^2, the diffuse reflectance measurements were 0.25 and 0.26 respectively. The LIPSS sample with the highest fluence of F = 3.4 J/cm^2 exhibited the highest diffuse reflectance spectra and at a wavelength of 900 nm, it showed a value of 0.26. The diffuse reflectance values were obtained from figure 18 (b).

In figures 18 (b), (e) and (h), the diffuse reflectance spectra are shown for a scanning velocity of v = 0.5 m/s, line spacing of 10 µm, 15 µm and 20 µm and at increasing fluence. The diffuse reflectance spectra increased with increasing laser fluence with the unirradiated sample spectra showing the lowest spectra and the sample with the highest fluence of 3.4 J/cm^2 showing the highest diffuse reflectance spectra. For varying line spacing, it was noted that the diffuse reflectance spectra increased as the line spacing was decreased. For these set of spectra, there were some visible spikes around wavelength values of 620 nm and 1150 nm which occurred on the unirradiated sample. These spikes were as well present on the samples irradiated with fluences of 0.8 J/cm^2 and 1.7 J/cm^2. These spiky features were however, absent for higher fluences of 2.4 J/cm^2 and 3.4 J/cm^2.

In figure 18 (b), the line spacing used was 10 µm. For this, the LIPSS with a fluence of 0.8 J/cm^2 unexpectedly portrayed the highest diffuse reflectance spectra for a wavelength range of 240 – 800 nm. In the higher wavelength range of 800 – 1300 nm, it however, showed the second lowest diffuse reflectance after the unirradiated sample and the sample with a fluence of 1.7 J/cm^2. At a line spacing of 15 µm (see figure 18 (e)), the highest fluence of 3.4 J/cm^2

showed the highest diffuse reflectance spectra in the lower wavelength range of 240 – 800 nm but at the higher wavelength, the fluence of 2.4 J/cm^2 showed the highest diffuse reflectance spectra. A spike was observed for only the sample with a fluence of 0.8 J/cm^2. Apart from the unusual spectra pattern observed here, the other fluences followed the general described pattern of low fluences producing low diffuse reflectance and vice versa especially in the high wavelength range.

Figure 18 (h) also showed a spike for only the sample with a fluence of 0.8 J/cm^2. The sample with a fluence of 1.7 J/cm^2 showed the highest diffuse reflectance spectra in the lower wavelength range. This then decreased even up to the extent of showing the lowest diffuse reflectance after the unirradiated sample at some higher wavelength range closer to 1300 nm. The other fluences once again showed the general pattern as described earlier.

For the specular reflectance spectra both the spiky and valley-like features appeared in this plot. The spikes occurred around a wavelength of 620 nm in relation to the unirradiated samples as well as the samples with fluences of 0.8 J/cm^2 and 1.7 J/cm^2 but were absent for the 2.4 J/cm^2 and 3.4 J/cm^2 samples. The valley-like features occurred for only the samples with fluences of 1.7 J/cm^2 through to a fluence of 3.4 J/cm^2 at a wavelength of 1150 nm. The valley-like features appeared at a wavelength of about 1150 nm for fluences of 0.8 J/cm^2 and 1.7 J/cm^2 in figure 18 (c). There was an additional valley-like feature which occurred for a fluence of 2.4 J/cm^2 in figure 18 (i).

Figures 18 (c), (f) and (i) represents the specular reflectance spectra for a scanning velocity of v = 0.5 m/s at line spacing of 10 µm, 15 µm and 20 µm respectively and at four different fluences. Figure 18 (c) shows the specular reflectance spectra for increasing fluences at a line spacing of 10 µm and a scanning velocity of 0.5 m/s. At a wavelength of 900 nm for fluences of 0.8 J/cm^2, 1.7 J/cm^2, 2.4 J/cm^2 and 3.4 J/cm^2, the corresponding specular reflectance values were 0.21, 0.11, 0.06 and 0.04 respectively. These values as well as the figures indicate that the specular reflectance spectra decrease with increasing laser fluence. The figures in general depict increasing specular reflectance spectra as the line spacing was increased.

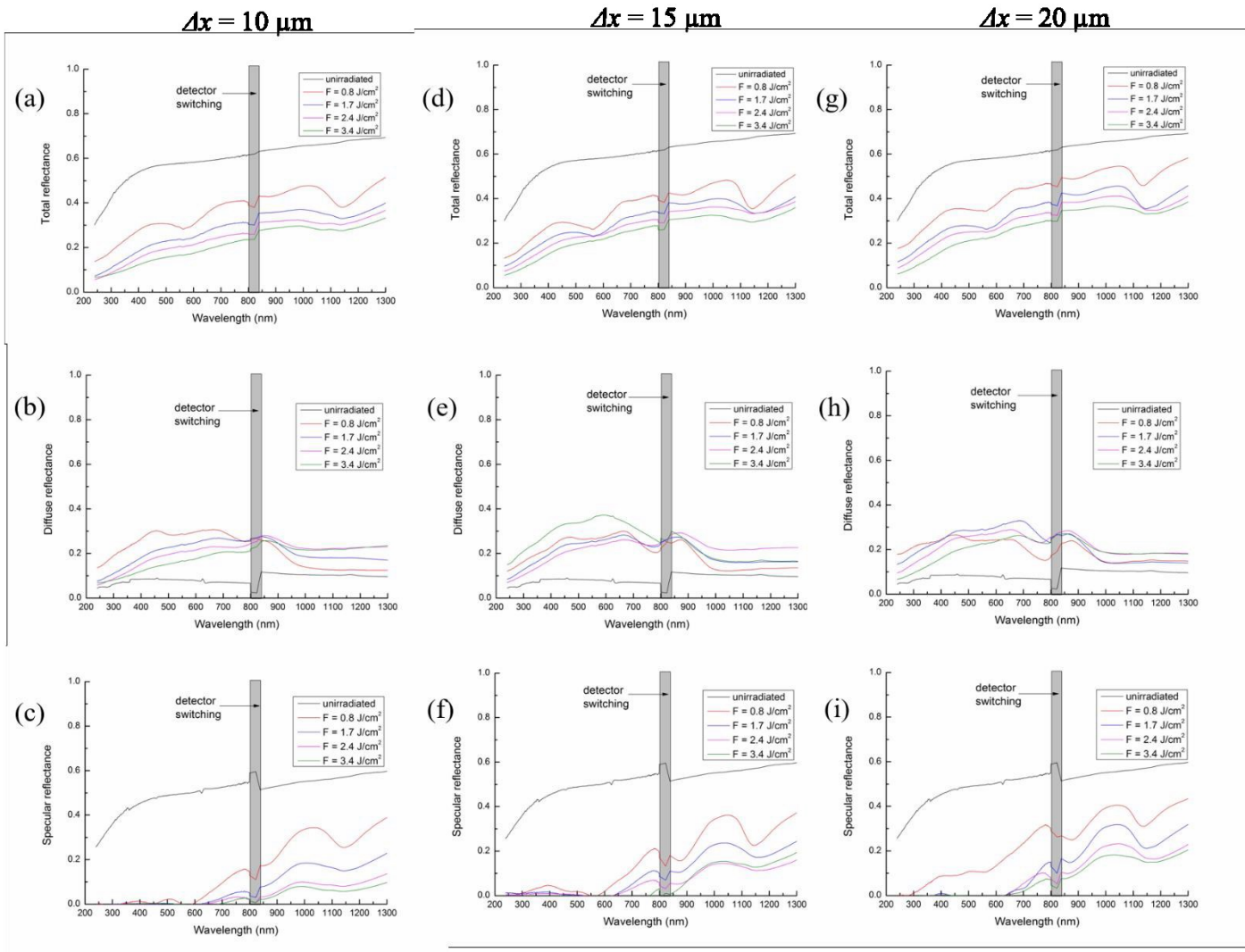

Figure 18: Reflectance plots as a function of wavelength for various LIPSS samples fabricated using different laser fluences of F = 0.8 J/cm², 1.7 J/cm², 2.4 J/cm² and 3.4 J/cm². (a), (b) and (c) show total, diffuse and specular reflectance plots respectively for samples with line spacing of Δx = 10 µm, (d), (e) and (f) show total, diffuse and specular reflectance plots respectively for samples with line spacing of Δx = 15 µm and (g), (h) and (i) show total, diffuse and specular reflectance plots respectively for samples with line spacing of Δx = 20 µm all at a scanning velocity v = 0.5 m/s. The grey rectangle indicates the detector switching point.

Figures 19 (a) - (c) and figures 18 (a) – (c) show the total, diffuse and specular reflectance spectra plots all at a line spacing of 10 µm with four different fluences of 0.8 J/cm², 1.7 J/cm², 2.4 J/cm² and 3.4 J/cm² but at scanning velocities of 1 m/s and 0.5 m/s respectively. At a glance of the two total reflectance spectra shown in figure 18 (a) and figure 19 (a) representing scanning velocities of 0.5 m/s and 1 m/s respectively, it can be noted that the LIPSS fabricated with a scanning velocity of 1 m/s shows higher total reflectance spectra compared to those fabricated at a scanning velocity of 0.5 m/s (highly blackened LIPSS) for all fluences. The valley-like features were absent at a fluence of 0.8 J/cm² for the sample fabricated with v = 1 m/s (see figure 19 (a)) but appeared deeply at the same fluence for v = 0.5 m/s (figure 18 (a)).

At a fluence of 1.7 J/cm^2, shallow valley-like features were seen on the samples with v = 0.5 m/s. A deep feature however, appeared for the sample with v = 1 m/s.

The diffuse reflectance spectra for samples fabricated with v = 0.5 m/s were observed to be in general higher as compared to those fabricated with v = 1 m/s as shown in figure 18 (b) and figure 19 (b). In figure 18 (b), there was a clear pattern in the diffuse reflectance in the lower wavelength range of 240 – 800 nm where the diffuse reflectance spectra increased with decreasing fluence which is once again a puzzling observation. In the higher wavelength range we however, observed that the lowest fluence of 0.8 J/cm^2 showed the lowest diffuse reflectance spectra after the unirradiated sample. There appeared a complete change in the spectra since the diffuse reflectance increased with increasing fluence in the higher wavelength range.

In figure 19 (b), the sample with fluence of 0.8 J/cm^2 showed a totally uncharacteristic behaviour when it showed the lowest diffuse reflectance at lower wavelengths and subsequently showed the highest diffuse reflectance at some wavelength in the higher wavelength region. The other three fluences actually showed decreasing diffuse reflectance for increasing fluences at the lower wavelength range and at the higher wavelength range; it portrayed increasing diffuse reflectance for increasing fluence. As already described for figure 18 (b), the diffuse reflectance increased with decreasing fluence in the lower wavelength range but increased with increasing fluence in the higher wavelength region.

With regards to the specular reflectance spectra at two different scanning velocities of v = 0.5 m/s and 1 m/s for four different fluences at the same line spacing of 10 µm, it was observed that the specular reflectance in the lower wavelength range was higher for v = 1 m/s (see figure 19 (c)) for a fluence value of 0.8 J/cm^2 when compared with specular reflectance of v = 0.5 m/s. The opposite is the case in the higher wavelength region where the lower scanning velocity showed a higher specular reflectance for the same lowest fluence used. For the other fluences, the specular reflectance was higher for v = 0.5 m/s in some wavelength range. At higher wavelengths of 1200 nm – 1300 nm, the samples with v = 1 m/s showed the highest specular reflectance spectra.

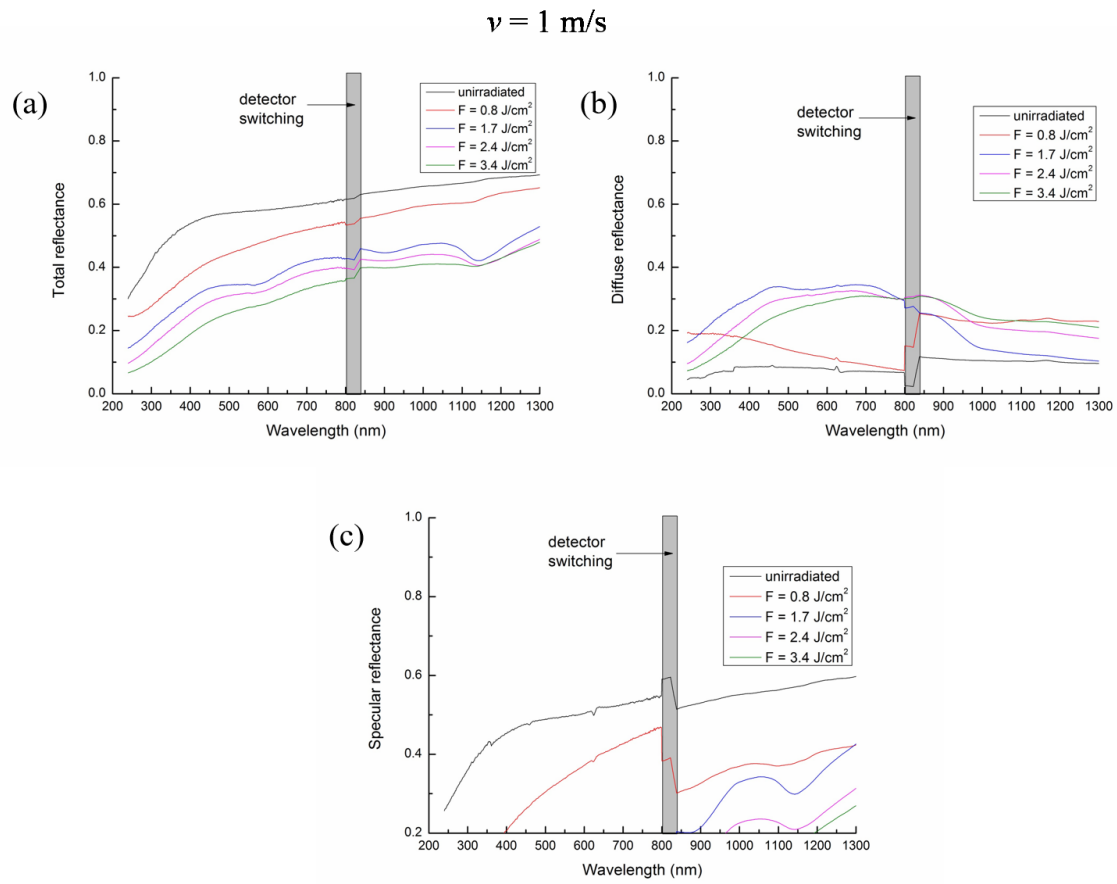

Figure 19: Total, diffuse and specular reflectance plots as a function of wavelength comparing LIPSS fabricated with line spacing of Δx = 10 µm but at four different fluences of F = 0.8 J/cm², 1.7 J/cm², 2.4 J/cm² and 3.4 J/cm². Scanning velocity of v = 1 m/s was used in the fabrication. The grey rectangle indicates the detector switching point.

5 DISCUSSION

The focus of this study was to generate Laser-induced periodic surface structures on stainless steel substrate materials utilising static linearly polarised femtosecond laser pulses and to characterise and investigate them with regards to their differing morphology, optical properties (reflectance, diffraction evolution) based on several parameters such as wavelength of the source of light, incidence angle, varying laser parameters: pulse fluence, number of pulse irradiation (scanning velocity). Therefore, in this section, the results of the various experiments performed are hereby discussed thoroughly in relation to previous knowledge (in terms of how the surface morphology of the irradiated stainless steel substrates relate to the optical properties). The relationship of the period of the various LIPSS samples with respect to the fabricating laser parameters is also investigated.

5.1 STRUCTURAL AND MORPHOLOGICAL FEATURES OF LIPSS

Laser fabricating parameters such as fluence, scanning velocity, line spacing, polarisation, and incident angle have significant effect on the structure and morphology of LIPSS. This in turn influences the periodicity of LIPSS. In this section, the effect of the various laser fabricating parameters utilised in the generation of the LIPSS samples are investigated thoroughly.

The naked eye inspection of the SEM micrographs displayed in (figures 13 (b), (d) and (f) representing a specific line spacing of 25 μm as well as in figures 13 (a), (c) and (e) representing a line spacing of 10 μm) at varying laser fluences portrays a pattern that the periodicity of the LIPSS increases with increasing laser fluences. These observations were further confirmed numerically by the performance of fast Fourier transforms on the SEM micrographs using the Gwyddion software. This occurs because as the laser fluences were increased the overlaps between adjacent laser spot kept diminishing and as a result closer LIPSS lines were generated. Further increase in the fluence then led to more crowded LIPSS with little spacing between them. This mechanism leads to the subsequent blackening of the LIPSS since several laser spots lie either on top of each other or with negligible spacing. As a result, the periodicity of LIPSS increases with increasing fluence for a fixed number of laser pulses or scanning velocity.

The observations made with regards to the relationship between the laser fluence and its corresponding LIPSS period agrees perfectly well with many other investigations which were done utilising several metals. A study conducted on tungsten W recognised that the periodicity of LIPSS increases with increasing laser pulse fluence for a fixed number of laser pulses [47]. Another study conducted on the dependency of LIPSS formation on fluence employed

molybdenum Mo, titanium Ti and platinum Pt as substrate materials. For all the cases considered, the periodicity increased with increasing fluence [61]. In Groenendijk and Meijer´s [23] studies, no relation between the laser fluence and the LIPSS period at normal incidence was detected upon investigation on stainless steel substrate material. There was however, a relationship between the periodicity of the LIPSS and the laser fluence when the samples were tilted. From the latter phenomenon as well as the earlier ones, it can thus be inferred that fluence plays a major role in the formation and selection of dominant LIPSS spacing.

The grating vectors for all the LIPSS samples generated in our experiment utilising static linear polarisation were orthogonal to the polarisation of the *E*-field vector. The LIPSSs were aligned vertical with respect to the *E*-field vector oriented parallel to *v* ($\alpha = 0°$). As a result, we can confidently say that almost all the LIPSS are LSFL in nature. The ratio Λ/λ in our experiment was in the range of 0.85 to 0.94 which agrees with literature values for LSFL [27]. Moreover, the theoretical period of Λ_{theor} = 1020 nm [27] is closer to the experimental mean value of about Λ_{exp} = 938 nm with the difference being as a result of the optical parameter changes in the stainless steel due to excitation of surface plasmons. The formation mechanism of these LSFL structures were as a result of the interference between the laser electric field and the surface electromagnetic waves generated upon irradiating the stainless steel samples with the laser [26].

Likewise it can be depicted from the SEM images and the calculation of the periods that as the line spacing decreases from 25 µm to 20 µm and also from 20 µm to 10 µm, there was an observation of a decreasing trend in the LIPSS period. As such, it is valid to say that for a fixed fluence, the period of LIPSS decreases with decreasing line spacing. When the overlap between adjacent laser spots increases, it leads to further sub divisions of the periodic patterns hence, it results in smaller LIPSS. This decrease in the LIPSS period is much pronounced when one observes the morphology from the SEM images for samples fabricated with line spacing of 10 µm and 25 µm but at a fluence of 1.7 J/cm^2 (see figure 13 (c) and (d)) and the other at a fluence of 6.6 J/cm^2 (see figure 13 (e) and (f)). Table 3 gives further information on the period of the SEM images.

There was evidence of the existence of another type of superposed structures (sub-LIPSS) in the case of the sample with a fluence of 0.8 J/cm^2 from a careful look at the SEM images from figure 13 (a). The sub-LIPSS (with grating vector also perpendicular to the laser polarisation) which can at a glance be observed to be having a period which is half of the initial LIPSS could

be said to be HSFLs. With all the samples fabricated using a fluence of 6.6 J/cm^2, there was a clear evidence of bifurcation of the main LIPSS into two or three separated lines. These bifurcations started at a fluence of 0.8 J/cm^2 for the LIPSS with the 10 μm line spacing. This further increased at 1.7 J/cm^2 and became more evident at a fluence of 6.6 J/cm^2. The bifurcations or sub-LIPSS were mainly evident at the peripheral region of the generated LIPSS. These observations can be explained on the basis of the increase of the laser intensity at higher laser fluence and also from the increase in the overlaps of the laser spots on the surface of the substrate material. These mechanisms then result in further decrease in the width of the already formed LIPSS and eventually leads to the mentioned bifurcation phenomenon. Some earlier investigations have confirmed this observation when the pulse fluence was varied while the pulse number of irradiation was kept constant. The bending and bifurcations observed was attributed to absorption peaks characterising efficacy factor η (k) at high excitation level [62]. In another study, redistribution of the electric field on metal surface was reported to be the major cause of the splitting of the initially formed LSFLs into HSFLs [63]. Similarly, from another report, as the number of pulse irradiation was increased HSFLs (observed mainly at the peripheral region of the ablation crater [64]) began to appear and even reached a point when its length was almost the same as that of the original LSFLs. These observations were all due to the fact that the field intensity increased and hence, the field intensity which was initially localised in the grooves became concentrated on the ridges in between the grooves. When the depth exceeded a critical value, it led to the ablation of the ridges in between the grooves hence, the formation of HSFLs [65]. Already, the effect of scanning velocity on femtosecond LIPSS has been investigated on stainless steel SS301L and Nickel Ni at a constant fluence [66]. It was observed that LSFL plays a major role for the formation of HSFL. With increasing scanning velocity, periodic nanostructures appeared on top of the ridges of LSFL and thus formed HSFL with twice the frequency of the LSFL. A separate study conducted on SS304 showed a distortion of the LIPSS with decreasing scanning velocity at a constant fluence. This led to the generation of some undulating grooves which appeared in a form perpendicular to the LIPSS orientation [23]. These explanations agree well with the investigations conducted in our study.

In our study, the periodicity of the LIPSS decreased from 900 nm to 820 nm and also from 960 nm to 859 nm by increasing the number of laser pulses from 2.4 to 4.8 at fluences of 0.8 J/cm^2 and 3.4 J/cm^2 respectively. This is in agreement with a study conducted on the effect of number of pulses on femtosecond LIPSS formation using platinum when an 800 nm fs laser was utilised [50]. The periodicity of LIPSS decreased from 620 nm to 550 nm when the

number of laser pulses increased from 30 to 500 at a constant fluence of 0.084 J/cm^2. Another investigation conducted on tungsten produced similar results. The fs LIPSS period decreased from 560 nm to 470 nm [67] and decreased from 600 nm to 350 nm [47] by increasing the number of pulses from 40 to 800 and from 100 to 10000 respectively. Further observations which proves that an increasing number of scans has a similar effect as a large number of pulses revealed the following: decreasing LIPSS periods were observed from 620 nm to 450 nm with increasing number of scans for a Magnesium Mg alloy (AZ31B) in air [68].

In figure 14, there was an increase of the number of laser pulses irradiation or a decrease in the scanning velocity on the stainless steel samples from $N = 1.0$ to $N = 9.6$ (from $v = 3$ m/s to $v = 0.2$ m/s) at a fluence of 2.0 J/cm^2. There was a general increase in the overlaps between the laser spots as the number of pulses was increased. As explained earlier, as the laser scanning velocity decreases many laser pulses hit a particular spot several times and this leads to the generation of deeper LIPSS. This subsequently results in the generation of many straight line patterns on the substrate material which further concentrates the LIPSS more closely. This leads to a general decrease in the period of the LIPSS at large N and these are evident from figures 14 and 15.

Clearer LIPSS pattern was noted to be due to the larger values of the electron-phonon energy coupling coefficient g. From studies, we can attribute the strong dependence of the depth and width of the ripples or gratings to the electron-phonon coupling strength and the electron diffusion [48].

From this study, the size of nanofeatures was observed to increase with increasing number of pulses at a given fluence. A similar trend was observed for a fixed number of laser pulses where the feature size increases with increasing fluence. Thus, the size and shape of nanostructures can be controlled by varying the fluence and the number of pulses. We can therefore confidently remark that the morphology of LIPSS strongly depends on laser parameters such as fluence, number of pulses, line spacing and the nature of the material. The period of LIPSS can be manipulated by the laser pulse energy (fluence) and the number of irradiated pulses in our case and in some other cases [47], the incident angle as well.

5.2 OPTICAL PROPERTIES INVESTIGATION

5.2.1 COLOURATION

Following the use of the LIPSS as gratings, the results obtained are hereby discussed in relation to laser parameters such as fluence, and line spacing as well as the diffraction angle, intensity, wavelength of the white light source and literature.

It has been well established from the graphical plots that LIPSS with higher fluence (energy, intensity) show a highly blackened surface morphology. As a result of the degree of blackness, the following remarks are worth making from the plots in figures 16 and 17: the absorption rate of the sample with a fluence of 6.6 J/cm^2 will be higher than that of the samples with fluences of 1.7 J/cm^2 and 0.8 J/cm^2 when light is incident on them. The wavelength increased for increasing diffraction angle for both fluences in figure 17 (a) and (b). However, the wavelength values for the corresponding diffraction angles were higher for the fluence value of 0.8 J/cm^2 as compared to the fluence of 1.7 J/cm^2. This also implies low period for the sample with low fluence and the inverse for the sample with high fluence. This could be interpreted from the fact that lower fluences implies less blackened surface as observed in the intensity against diffraction plot in figure 16. Hence, the colour effect could be said to be highly dependent on the laser fluence. A study conducted by [60] reveals similar results.

It should be noted that as the line spacing increases, the overlaps that exist between the fabricated LIPSS decrease (becomes narrow) and as such causes the energy flux to increase. This implies that the LIPSS fabricated using smaller line spacing would generate more energy concentration per spot (energy flux) with much deeper LIPSS. Hence, we would expect higher absorption (lower intensity) for such samples. This remark is noticeable from the intensity measurements displayed in figures 16 and 17. Comparing sample (0.8 J/cm^2, 25 μm) and sample (0.8 J/cm^2, 20 μm), the change in the wavelength values is more visible and pronounced as we observe lower wavelength for smaller line spacing at varying diffraction angle values. Correspondingly, this is also the case as we compare sample (0.8 J/cm^2, 20 μm) and sample (0.8 J/cm^2, 10 μm). Thus in general, higher wavelength values are obtained for larger line spacing of 25 μm and lower wavelengths values are obtained with regards to a line spacing of 10 μm (smaller) as illustrated in figure 17.

The results from figure 17 also confirm that larger LIPSS periods are obtained for larger line spacing and vice versa. This shows that the colour effect depends strongly on the line spacing as well. When the line spacing between the gratings increases, the period of the LIPSS likewise increases and vice versa. 10 µm spacing gives a period of about 875 nm, 20 µm implies 908 nm and 25 µm gives a period of 910 nm at a constant fluence of 0.8 J/cm^2. The diffracted light by the LIPSS (colour effects of LIPSS samples) depend strongly on the periods of the ripples [12]. They also depend on the diffraction angle β, light source direction (polarised or unpolarised) and on the ripple direction. The direction of the ripples was always perpendicular to the laser polarisation.

We can hereby confirm that surface structures aligned in arrays have a distinct feature of acting as surface gratings and hence can separate mixed "white light" into light of different wavelengths due to diffraction grating behaviour (the diffracted light by the ripples strongly depends on the light source direction and the orientation of the ripples as well). The colours are gradually changed from blue to red (spectral regions of colours firstly increase and then decrease with increasing spatial periods of the ripples induced by the laser radiation) due to the elongation of the diffracted light wavelengths. This unique effect of LIPSS on the optical properties can be seen even with the naked eyes. Moreover, variations in the periods of these structures resulted in an iridescent effect, as observed in peacock feathers, soap bubbles, films of oil and mother of pearl, because the reflected colour depends upon the viewing angle.

Furthermore, using the LIPSS samples as gratings in order to study the colour change effects, it has been established that colour effects depend strongly on the period of the LIPSS [12]. From this study therefore, the grating equation was obtained to be given by:

$$m\lambda = \Lambda(\sin\varphi \times \sin\alpha + \sin\beta) \tag{3}$$

where m is the order of diffraction, Λ is the period of the LIPSS, λ is the wavelength of the Xenon arc white light source, φ is the angle between the LIPSS to the x-axis and the detector, α is the angle of the LIPSS orientation to the z-axis and the incident light source and β is the diffraction angle.

This grating equation (3) agrees well with our studies but with some simplifications as a result of the parameters utilised during our experiment. Hence in our case, using mainly the first diffraction order $m = 1$, $\alpha = 0°$ and $\varphi = 90°$, our new equation is then given by:

$$\lambda = \Lambda \sin\beta \tag{4}$$

Using equation (4), the period of the LIPSS can be evaluated when the wavelength λ of the white light source reflected and the diffraction angle β are chosen from figure 17. Upon performing the various calculations, it was inferred that the period of the LIPSS samples were around 875 nm - 960 nm. From this calculation of the period, the relation between the laser fluence and the period of the LIPSS were again deduced to be in resonance with the experimental measurements of the period in this study (see table 3).

It should be noted that in situations where the gratings (LIPSS) are not oriented at an angle α of exactly 0° (in other words, the orientation of the LIPSS bends and hence it is not exactly perpendicular to the direction of the incident laser polarisation), as it appears in our case (a slight deflection in the angle say a tilt of about 1 – 3° maximum), there might just be some variations to equation (4). Some previous experimental works vividly illustrate that a single LIPSS line is not always straight [69, 70]. This tilt in our samples might have occurred during the fabrication process when the samples did not lie exactly at the designated position on the sample stage or perhaps during the characterisation and measurement of the diffraction pattern; a slight shift of the angle when the LIPSS samples were placed on the sample holder. Of course, the same argument about variation in equation (4) can be made when φ is not exactly 90°.

Figures 16 (a), (b) and (c) show two diffraction orders (first and second) of the grating-like LIPSS samples representing line spacing of Δx = 25 µm, 20 µm and 10 µm respectively. Figure 16 (a) with line spacing of Δx = 25 µm shows both first and second order diffraction peaks corresponding to various wavelengths. The first diffraction orders for diffraction angles β = 55° to 70° yielded wavelength values between 800 nm to 890 nm. The second order diffraction orders yielded peaks corresponding to wavelengths in the range of 400 nm to 445 nm. This wavelength range is about half the range of the corresponding first diffraction order wavelengths. There was a high intensity for the first diffraction order as compared to the intensity of the second diffraction order. As the diffraction angle increased from 55° to 70°, we observed a decrease in the intensity for both the first and second diffraction orders. This might have been due to the fact that less light was absorbed by the LIPSS as the diffraction angle increased and hence the detector just detected low intensities. This observation makes sense since at diffraction angle of 90°, almost no light would be incident on the LIPSS sample. Hence, almost nothing would be subsequently detected for such an orientation. For that matter, the wavelength would correspond exactly to the periodicity of the LIPSS. The second diffraction order peaks normally would yield lower intensities since most of the

incident light is absorbed in the first diffraction order. The second diffraction order peak might have occurred as a result of formation of some HSFLs due to nonlinear response of the surface structured with LSFLs which can be considered as the involvement of a second harmonic generation at the rough surface [48].

In figure 16 (b), there is an observation of some increment in the second diffraction order peaks. This might have occurred as a result of the reduction in intensity observed for the first diffraction order peaks. The first diffraction order could not absorb most of the light incident on it and hence this energy was directed to the second order diffraction. Again the wavelength was in the range of 790 nm to 890 nm for the first diffraction order and for the second diffraction order, 400 nm to 450 nm. Hence HSFLs occurrence can definitely be the reason for the observation of the second diffraction order peaks.

For the Δx = 10 μm line spacing displayed in figure 16 (c), the second diffraction order were greatly suppressed and hence are almost absent. Only the first diffraction order peaks are visible. The intensity for the first orders was very high and these were observed at a wavelength range between 775 nm and 875 nm for increasing diffraction angles β. The suppression of the second diffraction order might be as a result of the high intensities for the first diffraction orders. Additionally, higher diffraction orders are suppressed (in this case second order) and only the first diffraction order is present for sufficiently small nanograting period which coincidentally occurs at small line spacing. Figure 11 [12] shows a schematic diagram for the grating-like behaviour of LIPSS from which only two diffraction orders were actually visible because the others are all suppressed as a result of the high absorption level for the first and second diffraction orders and the period of the LIPSS. Third and higher diffraction order peaks were thus invisible in our investigations. With increasing line spacing, the diffraction patterns for the same fluence values increase. As such, we can remark that the colour effect also rely significantly on the line spacing.

Laser fabricating parameters (fluence and line spacing in this case) play significant roles with regards to the resulting nanograting shape or size (LIPSS morphology). The maximum achievable light absorption enhancement in nanograting (LIPSS) depends strongly on its morphological features. The subwavelength feature present on the nanograting structures enhances the light capture performance. Hence the absorption-enhancing performance differences might be due to the morphological feature differences in effective refractive indices of the nanogratings. At the same fluence of 0.8 J/cm^2, the ideal nanograting in our case was the

LIPSS sample fabricated with a line spacing of 25 µm (figure 16 (a)) hence both the first and second diffraction orders peaks appeared and the ratio of the intensity of the first to the second diffraction order peaks was higher than for the samples with the same fluence of 0.8 J/cm^2 but at different line spacing of 20 µm (figure 16 (b)) and 10 µm (figure 16 (c)). This shows that the light absorption enhancement factor LAEF increased rapidly with increasing line spacing. When the fluence was increased to 1.7 J/cm^2, the second order peaks disappeared. This indicates that a less perfect nanograting was generated at this fluence. The further decrease in the first diffraction order peaks at a fluence of 6.6 J/cm^2 confirms that an imperfect nanograting feature existed at this fluence. The light absorption enhancement therefore decreased with increasing fluence. This is in perfect agreement with the results reported in [71]. Figure 20 (a) exhibits the light absorption enhancement factor obtained from 980 nm MSM photodetector with a plasmonic grating structure. LAEF increased rapidly with decreasing aperture width (600 – 50 nm) [72]. In figure 20 (b), LAEF increased rapidly with increasing grating height [73].

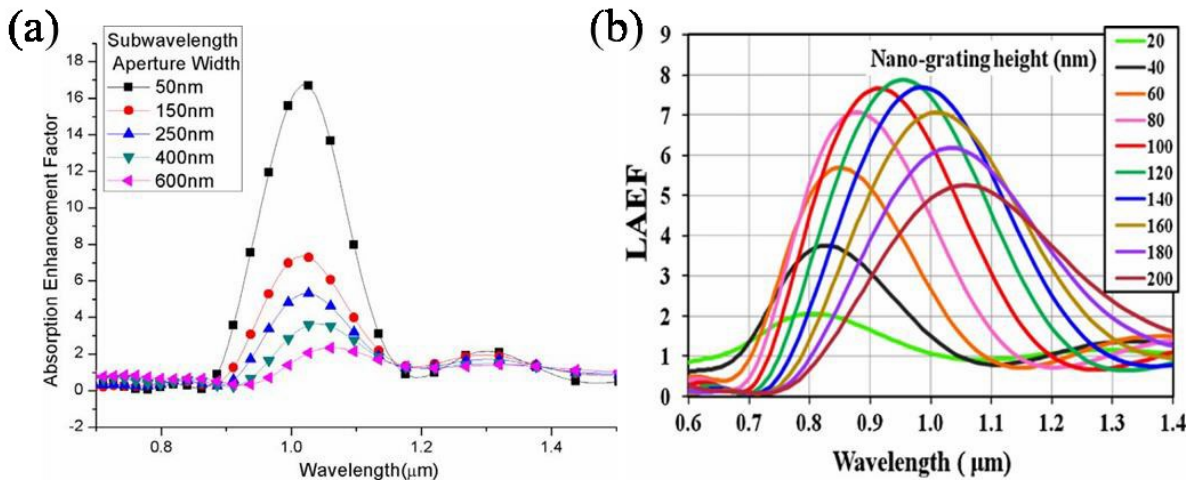

Figure 20: Absorption enhancement spectrum for different subwavelength aperture widths [72]. LAEF spectra for MSM-PDs with different nano-grating heights (20 nm - 200 nm) at aperture width of 100 nm [73].

These can further be explained on the basis of the following: the energy of light incident on the metal nanograting is coupled partially into propagating SPPs that can improve the light absorption efficiency in the subwavelength apertures present on the nanogratings. Hence, the absorption-improving effects of nanogratings are due to SPP-generated localized regions of the high-intensity electric field. The nanograting can therefore act as light concentrators (plasmonic lenses), which is essential for triggering the enhanced optical absorption of light inside the active regions of photodetectors [72].

With the investigation of the diffraction pattern performed by merely shining a monochromatic light unto the LIPSS samples, there is a significant amount of loss due to the non-confinement of the light beam and the substrate material. Using the integrating sphere for this investigation greatly improves the losses encountered. Measurement of a wide range of spectra could be enhanced for the diffraction pattern investigation when the distance from the detector to the LIPSS samples is widened. This ensures a wide range for the diffraction angles and hence a broader spectrum obtained. In our case, the distance between the detector and the LIPSS was enhanced to obtain a broad spectrum but this could be further optimised.

5.2.2 REFLECTANCE

From the results obtained from the use of the integrating sphere to characterise the LIPSS samples, the various reflectance plots (total, diffuse and specular reflectance spectra) are discussed in relation to fluence, line spacing, number of laser pulses or scanning velocity and the wavelength of the light source. This investigation using the integrating sphere with the spectrophotometer was performed only in the wavelength range of 240 - 1300 nm. The $BaS0_4$ white standard which happened to be coating of the integrating sphere employed in our reflectance measurements functions best in the wavelength range of 240 - 1600 nm hence the chosen range. The plotted curves discussed herein were all obtained from a vertical positioning of the LIPSS sample with respect to the sample holder and the detectors of the integrating sphere.

From the SEM images in figure 15, the LIPSS fabricated utilising a scanning velocity of v = 1 m/s (N = 2.4) displayed from (a) – (d) are observed to be less visible as compared to the LIPSS fabricated using a scanning velocity of v = 0.5 m/s (N = 4.8) displayed from (e) – (h). Several laser pulses per spot are deposited on the substrate material in the case of utilising low scanning velocity because in this structuring, the laser scanner moves relatively slower. This therefore ensures that a more blackened LIPSS is generated for low scanning velocities (large number of irradiated pulses). The phenomenon then yields higher absorption or low total reflectance and high diffuse reflectance values as is illustrated in figures 18 and 19.

In our investigations, it was observed that the reflectance of irradiated laser samples drops over the entire measured wavelength range when compared to the unirradiated polished stainless steel. The drop was more pronounced as the wavelength decreased. Measurements of the reflectance show a decrease in the total reflectance for the samples processed with higher laser fluence than for samples with low laser fluence. These observations agree with [60] and as a

result, it could be remarked that the spectral dependence observed can induce a greater absorption at blue and green wavelength range.

The unirradiated sample showed the highest total reflectance spectra since it portrays a mirror-like behaviour [74]. These obtained results were expected because the LIPSS with higher fluence values exhibited the most blackened LIPSS samples with the unirradiated and the samples irradiated with low fluences displaying less blackened surface morphologies. The low total reflectance values for the irradiated samples could also be explained on the basis of the multiple reflections from the irradiated surface of our LIPSS samples and a coincidental reduction in the light intensity at each reflection as a result of the finite value of reflectance of the LIPSS sample. Similar results were obtained in [40] (see figure 6) when the reflectance spectra dependence on fluence was investigated on stainless steel, brass and aluminium. In our case however, LIPSS (LSFLs) were generated and as such, the total reflectance measurement could only reach values in the range of 6.6 – 33.3 % as the wavelength increased from 240 nm to 1300 nm. This occured even at the highest fluence value of 3.4 J/cm^2, the lowest line spacing of 10 μm and at the lower scanning velocity of 0.5 m/s. Vorobyev and Guo [28] made a comparison between the total reflectance spectra of unirradiated and an unpolarised-light laser irradiated silver sample. It was realised that the laser unirradiated silver sample exhibited higher reflectance for the wavelength range considered. This is shown in figure 7 (a). Another investigation [29] showed that low total reflectance values around 5% was obtainable for black metals (Titanium, Platinum) and about 20% for black brass with the unirradiated samples yielding total reflectance values in the range of 70 - 95%. Figure 7 (b) illustrates this further. In these investigations, coral-like, spiky or groove structures were generated hence the extremely low reflectance values.

The results obtained from the diffuse reflectance spectra were expected since in general diffuse reflectance spectra compliments the specular as well as the total reflectance spectra measurements see figure 18 (a) - (i). It is well known that in diffuse reflectance, some of the back reflected light is absorbed by the sample and only the part scattered by the sample itself yields the diffuse reflectance spectra. Based on this, we can confiedently admit that the LIPSS with higher fluences will absorb most of the light beam incident on them. Hence, higher diffuse reflectance spectra are expected. Conversely, since the unirradiated sample behaves like a mirror, one would expect that there will be almost no absorption of light in this case. This therefore leads to very low diffuse reflectance spectra. It can therefore be concluded that diffuse reflectance increases with increasing laser fluence.

These results are in resonance with Lee et al [23, 30] experiments conducted on periodically textured stainless steel 430BA. On performing total and diffuse reflectance measurements on the samples, an inverse relationship was observed in the spectra for the total and diffuse reflectance measurements respectively (see figure 21).

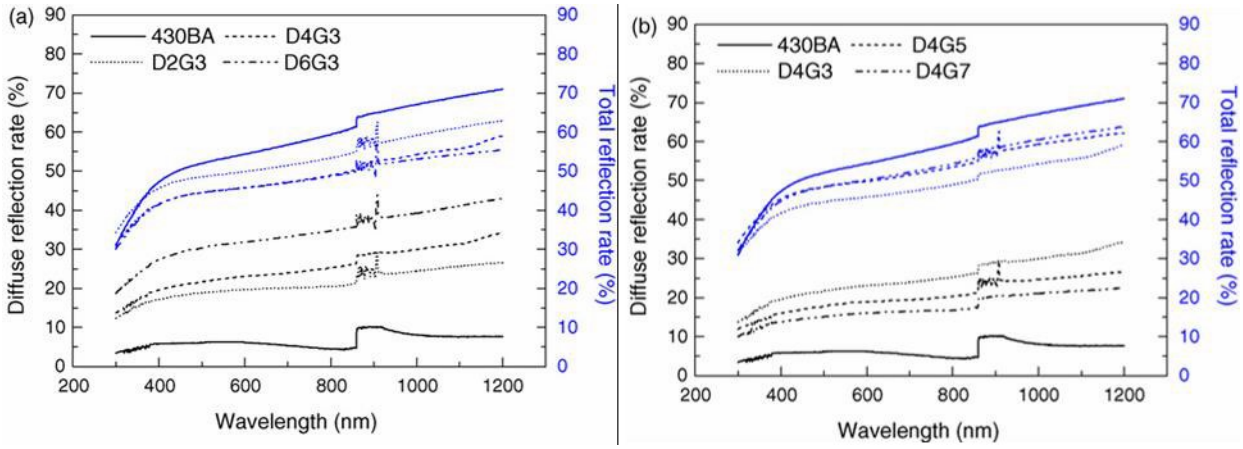

Figure 21: The TR and DR rates versus the wavelength curves for raw 430BA SS substrate at (a) different diameter and (b) different intervals of textured 430BA SS substrate [23].

The unirradiated sample with the smoothest and highly polished surface will definitely yield the highest specular reflectance since specular reflection in general occurs on smooth polished surfaces. As the roughness of the surface increases, the specular reflectance spectrum is expected to decrease. Irradiating the surface with higher fluences renders the surface granular or rough so to speak. This then leads to the results illustrated in figures 18 (b), (e) and (h).

Total reflectance decreased with decreasing line spacing for both low and high fluences. This behaviour can be explained in terms of the surface morphology of the LIPSS. The small line spacing generates large overlaps of the laser pulses and this leads to more pulses being deposited on the surface of the substrate material. This results in the generation of highly blackened LIPSS and therefore low reflectance is expected to be its hallmark.

At a line spacing of 10 µm, samples generated with $v = 1$ m/s (high scanning velocity) produced high total reflectance spectra for both low and high fluences. Total reflectance can thus be said to increase with increasing scanning velocity (see figure 19 (a)). The converse observation is illustrated in figure 18 (a) where $v = 0.5$ m/s and this yields low total reflectance. We note that as the scanning velocity at which the laser pulses irradiate the substrate material reduces, fewer pulses per spot hit the surface of the substrate. This then leads to the fabrication of not so pronounced blackened LIPSS (faint) hence the high total reflectance values.

We therefore expect similar results obtained for total reflectance investigation in terms of its relationship with parameters such as scanning velocity, fluence and line spacing for specular reflectance plots. The exact opposite relationship thus exists between the aforementioned laser parameters and diffuse reflectance as has been illustrated in figures 18 (b), (e) and (h) when the comparison between the three spectra was performed.

The puzzling change in the diffuse reflectance spectra at the low and high wavelength ranges might be due to the fact that the samples had not absorbed much of the light beam incident on them hence it was showing almost similar reflectance trend as observed in the total reflectance measurements. This subsequently changed to the normal diffuse reflectance spectra at high wavelength range since the sample had absorbed most of the light beam in that wavelength range. The sensitivity of the detector (the detector at the low wavelength range was less sensitive when compared with the detector at the high wavelength range of the integrating sphere) could also be another major factor that influenced this. As a result, a detector change ensured a rapid switch in the reflectance spectra for the diffuse as well as for some cases of the specular reflectance spectra. Again, low fluences implies the material possesses some energy closer to the material ablation threshold hence the material just undergoes minimal laser irradiation. The lower fluence irradiated material could therefore be likened to the unirradiated sample showing high total and specular reflectance but low diffuse reflectance.

The observed valley-like features at wavelengths of 580 nm and 1150 nm for the total reflectance spectra and at 1150 nm for the specular reflectance spectra as well as the spikes at a wavelength of 620 nm can all be attributed to the morphology of the LIPSS. The valley-like feature is absent at a wavelength of 620 nm for a fluence of 0.8 J/cm^2 but slightly visible at a wavelength of 1150 nm for a line spacing of 10 µm (Figure 18 (a)). For the other fluences, these valley-like features were present. Similar observations were made in relation to LIPSS fabricated with a line spacing of 20 µm. In figure 18 (a), the valley-like features were absent for a line spacing of 10 µm but were observed for only line spacing of 15 µm and 20 µm. It can thus be inferred that these features tend to disappear as the line spacing is decreased at higher fluences (3.4 J/cm^2 in our case). At the lowest fluence (0.8 J/cm^2), valley-like features were almost absent but was visible for all line spacing. It can thus be said that the valley- like feature appear for increasing fluence in the case of using a high scanning velocity of 1 m/s. The features can be said to rely strongly on the laser fabricating parameters and hence on the morphology of the LIPSS (see figure 20). In figure 18 (b) a sharp contrast was established between the scanning velocities. With $v = 0.5$ m/s, the valley-like features were observed for all line spacing

at the lowest fluence of 0.8 J/cm^2. The features were however absent at the highest fluence of 3.4 J/cm^2. The features in this scenario are present at low fluences but tend to disappear at high fluences.

Low fluences, large line spacing and high scanning velocity generated ideal gratings in this scenario since many deeper valley-like features appeared for these laser parameters. When the nanograting period is in the order of the light wavelength, the light wave may be resonant and reflects into the structure thereby resonant reflection occurs. Ideal nanogratings are therefore able to capture most of the reflecting light inside the active region of the substrate material. The subwavelength thus exhibit notable light transmission when surrounded by periodic nanostructures. External incident light is mostly harvested into the structures. This mechanism thus ensures that light is mostly re-emitted from a very small area surrounding the nanograting. This is associated with the properties of the Fabry-Perot cavity resonances for symmetric surface plasmon polaritons modes of the slits. The absorption enhancement caused by the excitation of SPPs is associated with the incident photons and their interaction with the nanogratings. Fabry-Perot like resonances are included in the transmission and absorption process through the subwavelength nanograting slits. The light absorption enhancement factor LAEF increases rapidly with the increase of the subwavelength line spacing and reduction in the fluence. The effective refractive index is a function of slit width for symmetrical SP modes when the slit experiences the incident wave. Therefore, with increasing the subwavelength line spacing, the effective refractive index increase [71, 72, 73] and leads to high light absorption enhancement feature. LAEF increases with the increase in the number of nanogratings. The increasing number of nanogratings enhances the effective propagation length of SPP wave. The SPP wave´s amplitude diminishes by the metal nanograting after reaching the subwavelength aperture.

6 CONCLUSION AND SUGGESTIONS FOR FUTURE WORK

In this master thesis, stainless steel was used as the substrate material on which LIPSS were fabricated utilising Yb:KYW thin disc fs laser which was operated at a fundamental wavelength of $\lambda = 1025$ nm. The goal of the study was to fabricate laser-induced periodic surface structures on stainless steel substrate material using static linearly polarised fs laser pulse and then to investigate the optical properties. The colour effect was thus investigated following the utilisation of the LIPSS as grating-like structures. The reflectance (total, diffuse and specular) spectra were also studied following the use of various laser parameters in the fabrication of LIPSS.

It was established that laser parameters such as fluence, number of irradiated pulses (scanning velocity) as well as line spacing play significant roles on the periodicity of LIPSS. The periodicity of LIPSS increased from 820 to 920 nm and from 879 to 960 nm with increasing fluence at a fixed scanning velocity of 0.5 m/s and 1 m/s respectively. Also, at a fluence of 0.8 J/cm^2, the periodicity increased from 820 to 900 nm for increasing line spacing and at F = 3.4 J/cm^2, the periodicity again increased from 859 to 960 nm for increasing line spacing. Thus the morphological feature investigations proved that laser parameters and the nature of the substrate material control the size and shape of the resulting nanofeatures. Clearer LIPSS pattern from our studies were noted to be as a result of larger values of the electron-phonon energy coupling coefficient g. Surface property behaviour of LIPSS (highly visible LIPSS in this case) subsequently showed low intensity as well as low total reflectance values (optical properties) proving that the optical properties rely strongly on the morphology of LIPSS. Sub LIPSS observed at the peripheral region of the initial LSFLs led to the formation of HSFLs and this illustrates that at low fluences and smaller line spacing HFSLs can emerge from LSFLs. The formation mechanism here was attributed to the increase in the laser field intensity which was initially localised in the grooves but eventually became concentrated on the ridges in between the grooves and hence the formation of the sub LIPSS. It was also explained based on the absorption peaks characterisng efficacy factor at high excitation level.

Furthermore, we can conclude that the colour effect variation arise as a result of the morphological features on the various LIPSS samples, orientation of LIPSS and the viewing angle. From that it was noted that the diffraction pattern depend strongly on the periodicity of the LIPSS. At larger diffraction angles, the periodicity of LIPSS increased with decreasing intensity. Additionally, the suppression of higher diffraction orders (second order in our case)

was attributed to the sufficiently small nanograting periods as well as the absorption of most of the light intensities by the higher diffraction orders. Laser parameters like fluence and line spacing greatly controlled the colour effect behaviour of the grating-like LIPSS. From our study, low fluence but large line spacing displayed the ideal grating behaviour. Increasing the fluence for the same large line spacing results in a less ideal grating behaviour. Similarly, a reduction in the line spacing for a fixed low fluence yields a non-ideal grating behaviour. The ideal grating from our studies subsequently yields high LAEF. And this comes as a result of high effective refractive indices through the enhancement of the light interaction of subwavelength nanogratings with SPPs.

The total and specular reflectance spectra decreased with increasing fluence but increased with increasing scanning velocity as well as line spacing. On the contrary, diffuse reflectance increased with increasing fluence but decreased with increasing scanning velocity and line spacing. Thus total, specular as well as diffuse reflectance were observed to be highly dependent on the surface morphology of LIPSS hence any change in the laser fabricating parameters will lead to a change in the spectra. Higher laser fluences were observed to effect a significant improvement in the diffuse reflectance of light. This phenomenon as already known can greatly enhance the blackening of metals which is a requirement for solar cell application (photovoltaic industry). Ideal grating behaviour was observed for a fluence of $F = 0.8$ J/cm^2, line spacing of 20 µm and at a scanning velocity of 1 m/s. LAEF was higher for the ideal nanograting parameters. This high absorption is due to the increase in the effective refractive index as well as Fabry-Perot like resonances from subwavelength nanogratings light interactions with SPPs.

Other polarisation states especially dynamic polarisation should be employed in this investigation to further explore the dependence of surface morphological effect on the reflectance of LIPSS. In the integrating sphere investigations, it would be interesting to utilise a polarised light source in horizontal and vertical orientation as well as an unpolarised light source so as to further confirm and ascertain the effect of polarisation on the LIPSS samples. The absorptance of the LIPSS sample could also be directly measured by positioning the sample in the centre of the integrating sphere with the support of a “centre mount”. Another effect that can generate some variations in the morphological features and hence the reflectance spectra is to use different ambient gases in the fabrication of LIPSS. This thus effects a slight change in the refractive index via plasma effects on the substrate material.

Other possibilities may include using a polarised light source in the diffraction pattern (colour effect) investigation of LIPSS. The second harmonic wavelength together with the fundamental wavelength could also be employed the dependence of LIPSS on varied wavelength. Utilising different substrate material that are optically useful such as fused silica could perhaps help to fathom the diffraction order properties. As a result of its transparent nature and large period based on the wavelength of the fabricating laser, more diffraction orders could be generated. It will be equally interesting to observe the various reflectance measurements with the integrating sphere from LIPSS fabricated on fused silica. To obtain a wide wavelength range for study of the reflectance on LIPSS fabrication, an integrating sphere coated with a standard material that spans through the UV, Vis and IR wavelength range should be employed. This is necessary and should be performed due to the narrow wavelength range which accompanied the $BaSO_4$ investigation.

7 REFERENCES

1. **Vorobyev A. Y. and Guo C.**, *Femtosecond laser blackening of platinum*, **J. Appl. Phys. 104, 053516 (2008)**.
2. **Ardron M., Weston N. and Hand D.**, *A practical technique for the generation of highly uniform LIPSS*, **Appl. Surf. Sci. 313, (2014) 123–131**.
3. **Birnbaum M.**, *Semiconductor surface damage produced by ruby lasers*, **J. Appl. Phys. 36 (11), (1965) 3688–3689**.
4. **Vorobyev A. Y. and Guo C.**, *Effects of nanostructure-covered femtosecond laser-induced periodic surface structures on optical absorptance of metals,* **Appl. Phys. A, 86, (2007) 321-324**.
5. **Shen M., Carey J. E., Crouch C. H., Kandyla M., Stone H. A. and Mazur E.,** *High-density regular arrays of nanometer-scale rods formed on Silicon surface via femtosecond laser irradiation in water,* **Nano Lett., 8, (2008) 2087-2091.**
6. **Kumar B. and Soni R. K.,** *Submicometre periodic surface structures in InP induced by nanosecond UV laser pulses,* **J. Phys. D: Appl. Phys., 41, (2008) 155303**.
7. **Simova E., Hnatovsky C., Taylor R. S., Rayner D. M. and Corkum P. B.**, *Proc. Photon Processing in Microelectronics and Photonics VI*, **San Jose, CA, (2007) p.64581B.**
8. **Bonse J., Sturm H., Schmidt D. and Kautek W.,** *Chemical, morphological and accumulation phenomena in ultrashort-pulse laser ablation of TiN in air,* **Appl. Phys. A, 71, (2000) 657-665. 4.**
9. **Baudach S., Bonse J. and Kautek W.,** *Ablation experiments on polyimide with femtosecond laser pulses,* **Appl. Phys. A, 69, (1999) S395-S398.**
10. **Sipe J. E., Young J., Preston J. and van Driel H.,** *Laser-induced periodic surface structure. I. Theory,* **Phys. Rev. B, 27, (1983) 1141-1154.**
11. **Guo C. F., Sun T.Y., F. Cao, Liu Q., Ren Z. F.**, *Metallic nanostructures for light trapping in energy-harvesting devices*, **Light-Sci. Appl. 3 (2014) e161.**
12. **Li G., Li J., Hu Y., Zhang C., Li X., Chu J., Huang W.**, *Femtosecond laser color marking stainless steel surface with different wavelengths*, **Appl. Phys. A 118 (2015) 1189–1196.**
13. **Fadeeva E., Schlie S., Koch J., Ngezahayo A., Chichkov B. N.**, *The hydrophobic properties of femtosecond laser fabricated spike structures and their effects on cell proliferation*, **Phys. Status Solidi A 206 (2009) 1348-1351.**

14. **Vorobyev A. Y., Makin V. S. and Guo C.,** *Brighter light sources from black metal: significant increase in emission efficiency of incandescent light sources,* **Phys. Rev. Lett., 102, (2009) 234301.**
15. **Eichstädt J., Römer G. R. B. E. and Veld A. J. H. it., Phys. Procedia, 12, Part B, (2011) 7-15.**
16. **Hwang T. Y., Vorobyev A. Y. and Guo C.,** *Surface-plasmon-enhanced photoelectron emission from nanostructure-covered periodic grooves on metals,* **Phys. Rev. B, 79, (2009) 085425.**
17. **Schlie S., Fadeeva E., Koroleva A., Ovsianikov A., Koch J., Ngezahayo A., Chichkov B. N.,** *Laser-based nanoengineering of surface topographies for biomedical applications*, **Photonic Nonostruc. 9 (2011) 159-162.**
18. **Vorobyev A.Y. and Guo C.,** *Colorizing metals with femtosecond laser pulses*, **Appl. Phys. Lett. 92, 041914 (2008).**
19. **Sipe J. E., Young J. F., Preston J. S., and van Driel H. M.,** *Laser-induced periodic surface structure. I. Theory*, **Phys. Rev. B 27 (2), (1983) 1141–1154.**
20. **Nathala C. S. R., Ajami A., Ionin A. A., Kudryashov S. I., Makarov S. V., Ganz T., Assion A., Husinsky W.,** *Experimental study of fs-laser induced sub-100 nm periodic surface structures on titanium*, **Optics Express 5915 (2015), Vol. 23, No. 15.**
21. **Yao J. W., Zhang C. Y., Liu H. Y., Dai Q. F., Wu L. J., Lan S., Gopal A. V., Trofimov V. A., and Lysak T. M.,** *High spatial frequency periodic structures induced on metal surfaces by femtosecond laser pulses*, **Optics Express 905, Vol. 20, No. 2 (2012).**
22. **Gecys P., Vinciunas A., Gedvilas M., Kasparaitis A., Lazdinas R. and Raciukaitis G.,** *Ripple formation by femtosecond laser pulses for enhanced absorptance of stainless steel*, **Journal of Laser Micro/Nano-engineering Vol. 10, No 2, 2015.**
23. **Groenendijk M., Meijer J.,** *Microstructuring using femtosecond pulsed laser ablation*, **J. Laser Appl. 2006, 18, 227–235.**
24. **Lee S. J., Chen S. L., Peng C. W., Lin C. Y., Ke W. C.,** *Enhanced diffuse reflection of light into the air using silver coating periodically textured 430BA Stainless steel substrate,* **Materials Chemistry and Physics 118 (2009) 219-222.**
25. **Huang M., Zhao F., Cheng Y., Xu N. and Xu Z.,** *Origin of laser-induced near subwavelength ripples: interference between surface plasmons and incident laser*, **ACS, Nano Vol. 3. No 12, 4062-4070.**

26. **Jin Y., Allegre O. J., Perrie W., Abrams K., Ouyang J., Fearon E., Edwardson S. P., Dearden G.,** *Dynamic modulation of spatially structured polarization fields for real-time control of ultrafast laser-material interactions*, **Opt. Express 21 (2013) 25333-25343.**

27. **Gräf S. and F.A. Müller,** *Polarisation-dependent generation of femtosecond laser-induced periodic surface structures*, **Appl. Surf. Sci. 331 (2015) 150-155.**

28. **Vorobyev A. Y. and C. Guo,** *Spectral and polarisation responses of femtosecond laser-induced periodic surface structures on metals*, **J. Appl. Phys. 103, 043513 (2008).**

29. **Vorobyev A. Y. and C. Guo,** *Multifunctional surfaces produced by femtosecond laser pulses*, **J. Appl. Phys. 117, 033103 (2015).**

30. **Lee S. J. and W.C. Ke,** *Enhanced Diffuse Reflection of Light by Using a Periodically Textured Stainless Steel Substrate*, **Solar Cells – Thin Film Technologies (2011) 39 - 54.**

31. **Colombier J. P., Garrelie F., Faure N., Reynaud S., Bounhalli M., Audouard E., Stoian R.,** *Effects of electron-phonon coupling and electron diffusion of ripples growth on ultrafast laser irradiated metals*, **J. Appl. Phys. 111(2) 024902 (2012).**

32. **Guan Y. C., Zhou W., Li Z. L., Zhang H. Y., Lim G. C., and Hong M. H.,** *Femtosecond laser-induced ripple structures on magnesium*, **Appl. Phys. A (2014) 115: 13-18.**

33. **Jia T. Q., Chen H. X., Huang M., Zhao F. L., Qiu J. R., Li R. X., Xu Z. Z., He X. K., Zhang J., and Kuroda H.,** *Formation of nanogratings on the surface of a ZnSe crystal irradiated by femtosecond laser pulses*, **Phys. Rev. B 72(12), 125429 (2005).**

34. **Le Harzic R., Dörr D., Sauer D., Stracke F., and Zimmermann H.,** *Generation of high spatial frequency ripples on silicon under ultrashort laser pulses irradiation*, **Appl. Phys. Lett. 98(21), 211905 (2011).**

35. **Ursu I., Mihăilescu I. N., Popa Al., Prokhorov A. M., Ageev V. P., Gorbunov A. A., and Konov V. I.,** *Studies of the change of a metallic surface microrelief as a result of multiple-pulse action of powerful UV laser pulses*, **J. Appl. Phys. 58, 3909 (1985).**

36. **Das S. K., Messaoudi H., Debroy A., McGlynn E. and Grunwald R.,** *Multiphoton excitation of surface plasmon-polaritons and scaling of nanoripple formation in large band gap materials,* **Opt. Mater. Express, 3, 1705-1715 (2013).**

37. **Vorobyev A. Y., and C. Guo,** *Direct creation of black silicon using femtosecond pulses*, **Appl. Surf. Sci. 257 (2011) 7291 – 7294.**

38. **Huang H., Yang L. M., Bai S., and Liu J.,** *Blackening of metals using femtosecond fiber laser*, **Appl. Opt. 54 (2015) 324 – 333.**
39. **Clark S. E.and D. C. Emmony,** *Ultraviolet-laser-induced periodic surface structures*, **Physical Review B, Vol. 40, No. 4 (1989) 2031-2041.**
40. **Ou Z., Huang M., Zhao F.,** *The fluence threshold of femtosecond laser blackening of metals: The effects of laser-induced ripples,* **Optics and Laser Tech. 79 (2016) 79-87.**
41. **Lu Y. F. and W. K. Choi,** *Controllable laser-induced periodic surfaces of silicon-dioxide/silicon interface by excimer laser irradiation*, **J. Appl. Phys. 80 7052-6 (1996).**
42. **Fauchet P. M.and A. E. Siegman,** *Surface ripples on silicon and gallium arsenide under picosecond laser illumination*, **Appl. Phys. Letters 40, 824 (1982) 823-826.**
43. **Liu Y., Brelet Y., He Z., Yu L., Forestier B. et al,** *Laser-induced periodic annular surface structures on fused silica surface*, **Appl. Phys. Lett. 102, 251103 (2013).**
44. **Siegman A. E., and P. M. Fauchet,** *Stimulated wood´s anomalies on laser-illuminated surfaces*, **IEEE Journal of Quantum Electronics, Vol. QE-22, No. 8 (1986) 1384 -1403.**
45. **Vorobyev A. Y. and C. L. Guo,** *Metal colorization with femtosecond laser pulses, In Proceedings of SPIE on High-Power Laser Ablation VII*, **Taos, NM, USA, 20–24 April 2008.**
46. **Nayak B. K. and M. C. Gupta,** *Ultrafast laser-induced self-organized conical micro/nano surface structures and their origin*, **Opt. Lasers Eng. 2010, 48, 966–973.**
47. **Zhao Q. Z., Malzer S., Wang L. J.,** *Formation of subwavelength periodic structures on tungsten induced by ultrashort laser pulses*, **Opt. Lett. 2007, 32, 1932–1934.**
48. **Keilmann F. and Y. H. Bai,** *Periodic surface structures frozen into CO2 Laser-melted quartz,* **Appl. Phys. A. 29, 9 (1982).**
49. **Ruiz de la Cruz A., Lahoz R., Siegel J., de la Fuente G. F., and Solis J.,** *High speed inscription of uniform, large-area laser-induced periodic surface structures in Cr films using a high repetition rate fs-laser*, **Opt. letters 39 (2014) 2491-2494.**
50. **Vorobyev A. Y., Markin V. S., Guo C. L.,** *Periodic ordering of random surface nanostructures induced by femtosecond laser pulses on metals,* **J. Appl. Phys. 101 (2007) 034903.**
51. **Wang J. C. and C. L. Guo,** *Formation of extraordinarily uniform periodic structures on metals induced by femtosecond laser pulses,* **J. Appl. Phys. 100 (2006) 023511.**

52. **Vorobyev A. Y., Guo C. L.,** *Femtosecond laser-induced periodic surface structure formation on tungsten,* **J. Appl. Phys. 104 (2008) 063523.**

53. **Bashir S., Rafique M. S., Husinsky W.,** *Femtosecond laser-induced subwavelength ripples on Al, Si, CaF2 and CR-39,* **Nucl. Instrum. Meth. B 275 (2012) 1 - 6.**

54. **Miyaji G., Miyazaki K.,** *Origin of periodicity in nanostructuring on thin film surfaces ablated with femtosecond laser pulses,* **Opt. Express 16 (2008) 16265 – 16271.**

55. **Tavera T., Perez N., Rodriguez A., Yurrita P., Olaizola S. M., and Catano E.,** *Periodic patterning of silicon by direct nanosecond laser interference ablation***, Appl. Surf. Sci. 258 (2011) 1175 – 1180.**

56. **Springsteen A.,** *Reflectance Spectroscopy: An overview of classification and Techniques,* **193 – 224.**

57. **Parretta A., Yakubu H., Ferrazza F.,** *Method for measurement of the hemispherical/hemispherical reflectance of photovoltaic devices***, Optics Communications 194 (2001) 17-32.**

58. **Peters M., Ulbrich C., Goldschmidt J. C., Fernandez J., Siefer G., Bläsi B.,** *Directional selective trapping in a germanium solar cell,* **Opt. Exp. A136 Vol. 19 No. S2 (2011).**

59. **PIKE Technology,** *Diffuse Reflectance – Theory and Applications,* **PIKE Technologies © (2011) 1-2.**

60. **Hou S., Huo Y., Xiong P., Zhang Y., Jia T., Sun Z., Qiu J. and Xu Z.,** *Formation of long- and short- periodic nanoripples on stainless steel irradiated by femtosecond laser pulses***, Appl. Phys. 44 (2011) 505401 (7pp).**

61. **Okamuro, K., Hashida, M., Miyasaka, Y.; Ikuta, Y., Tokita, S., Sakabe, S.,** *Laser fluence dependence of periodic grating structures formed on metal surfaces under femtosecond laser pulse irradiation,* **Phys. Rev. B 2010, 82, 165417.**

62. **He S., Nivas J. J., Anoop K. K., Vecchione A., Hu M., Bruzzese R., and Amoruso S.,** *Surface structures induced by ultrafast laser pulses: Formation mechanisms of ripples and groves***, Appl. Surf. Sci. 353 (2015) 1214 – 1222.**

63. **Jia T. Q., Chen H. X., Huang M., Zhao F. L., Qiu J. R., Li R. X., Xu Z. Z., He X. K., Zhang J., and Kuroda H.,** *Formation of nanogratings on the surface of a ZnSe crystal irradiated by femtosecond laser pulses***, Phys. Rev. B 72(12), 125429 (2005).**

64. **Obara G., Maeda N., Miyanishi T., Terakawa M., Nedyalkov N. N., and Obara M.,** *Plasmonic and Mie scattering control of far-field interference for regular ripple formation on various material substrates*, **Opt. Express 19 (20), 19093–19103 (2011).**

65. **Vorobyev A.Y., Guo, C.L.,** *Femtosecond laser-induced periodic surface structure formation on tungsten,* ***J. Appl. Phys.*** **2008,** ***104*****, 063523.**

66. **Iyengar V. V., Nayak B. K., More K. L., Meyer H. M., Biegalski M. D., Li J. V., and Gupta M. C.,** *Properties of ultrafast laser textured silicon for photovoltaic*, **Solar Energy Materials and Solar cells 95 (2011) 2745 – 2751.**

67. **Guan, Y.C., Zhou, W., Li, Z.L., Zheng, H.Y.,** *Femtosecond laser-induced iridescent effect on AZ31B magnesium alloy surface,* ***J. Phys. D Appl. Phys.*** **2013,** ***46*****, 425305.**

68. **Hwang T. Y. and C. L. Guo,** *Angular effects of nanostructure-covered femtosecond laser induced periodic surface structures on metals*, **J. Appl. Phys. 2010, 108, 073523.**

69. **Iyengar V. V., Nayak B. K., Gupta M. C.,** *Optical properties of silicon light trapping structures for photovoltaics*, **Solar Energy Materials and Solar cells 94 (2010) 2251 – 2257.**

70. **Ansan M. S. and M. S. Lee,** *Formation mechanism of self-organised nanogratings on a titanium surface using femtosecond laser pulses*, **Optical Engineering, Ronald G. Driggers, 51 (12) 121815 (2012).**

71. **Das N., Karar A., Vasiliev M., Tan C. L., Alameh K., Lee Y. T.,** *Analysis of nano-grating-assisted light absorption enhancement in metal-semiconductor-metal photodetectors patterned using focused ion-beam lithography,* **Opt. Comm. 284 (2011) 1694 – 1700.**

72. **Tan C. L., Lysak V. V., Alameh K., Lee Y. T.,** *Absorption enhancement of 980 nm MSM photodetector with a plasmonic grating structure,* **Optics Communications 283 (2010) 1763 – 1767.**

73. **Masouleh F. F., Das N., Mashayekhi H. R.,** *Optimization of light transmission efficiency for nano-grating assisted MSM-PDs by varying physical parameters,* **Photonics and Nanostructures – Fundamentals and Applications 12 (2014) 45 – 53.**

74. **Parretta A., Sarno A., Tortora P., Yakubu H., Maddalena P., Zhao J., and Wang A.,** *Angle-dependent reflectance measurements on photovoltaic materials and solar cells*, **Optics Communications 172, 139-151 (1999).**

LIST OF FIGURES

LIST OF TABLES

ABBREVIATIONS

LIPSS …… Laser-induced periodic surface structures

LSFL ……. Low spatial frequency LIPSS

HSFL ……. High spatial frequency LIPSS

fs …… femtosecond

SPP …… surface plasmon polariton

SLM …….. spatial light modulator

MEMS …….. micro-electro-mechanical systems

SEM …….. scanning electron microscopy

FFT ……... fast Fourier transform

PMT …….. photomultiplier

UV ……. ultraviolet

Vis ……. visible

NIR ……... near infra-red

MSM ……. Metal semiconductor metal

PD ……. Photodetector

LAEF …… light absorption enhancement factor

ABBREVIATIONS

LIPSS …… Laser-induced periodic surface structures

LSFL ……. Low spatial frequency LIPSS

HSFL ……. High spatial frequency LIPSS

fs …… femtosecond

SPP …… surface plasmon polariton

SLM …….. spatial light modulator

MEMS …….. micro-electro-mechanical systems

SEM …….. scanning electron microscopy

FFT ……... fast Fourier transform

PMT …….. photomultiplier

UV ……. ultraviolet

Vis ……. visible

NIR ……... near infra-red

MSM ……. Metal semiconductor metal

PD ……. Photodetector

LAEF …… light absorption enhancement factor

ACKNOWLEDGEMENTS

To begin with, I am grateful for the opportunity given me by Prof. Müller to conduct my master thesis in his working group. For that honour done me, I say a big thank you. I also want to appreciate the assistance of my second mentor, Dr. Stephan Gräf for his availability in discussing the progress of my work. For his constructive criticisms, healthy working relationship and his sense of direction which enabled me to finish this work.

This thesis was conducted with the immense support and contribution of Clemens Kunz, a PhD student in the working group. I want to use this platform to express my sincere appreciation for his input with regards to the experimental procedures and succinct clarifications of certain stuff.

Next, I want to thank Andre Kramer for his assistance in some of the experimental works. Special thanks goes to Christoph Wenisch and Sebastian Engel for helping me in setting up the experimental setup for the diffraction pattern measurements. I am equally grateful to Dr. Michael Kräcker who offered a helping hand which eased the integrating sphere measurements of our LIPSS samples.

To the members of the working group, I am highly indebted for your hospitality, friendliness, accommodating and cordial working relationship.

My heartfelt appreciation goes to my family especially my mother, Madam Grace Augustina Quansah for her continued support throughout my education, in particular my master studies. Your motivation and prayers spurred me on to achieve this laurel.

Finally, to my friends, church members, programme mates and colleagues I say a big thank you for your continued encouragement and prayers.

Last but not least, I want to appreciate Vivian Augusta for her continued belief in me, your care and inspiration has brought me this far.

STATUTORY DECLARATION

I, Theophilus Kobina Sarpey hereby declare that this work was independently written with no form of support from any individual other than the specified sources and aids stated. The citation of information, words and ideas from the various sources are clearly provided in this document.

_____ _____

Place, Date of delivery Signature of the author

On the part of the author, there is no objection to provide this present thesis for public use in the Thuringian University and State Library. I further agree that permission for extensive copying of this thesis for scholarly purposes may be granted by the head of my department or by his/her representatives. It is understood that copying or publication of this thesis for financial gain shall not be allowed without the author´s written permission.

_____ _____

Place, Date Signature of Trust